Comprehensive H$_2$/O$_2$ Kinetic Model for High-Pressure Combustion

MICHAEL P. BURKE,[1] MARCOS CHAOS,[2] YIGUANG JU,[1] FREDERICK L. DRYER,[1] STEPHEN J. KLIPPENSTEIN[3]

[1]*Department of Mechanical and Aerospace Engineering, Princeton University, Princeton, NJ 08544*
[2]*Fire and Explosions Dynamics Group, Fire Hazards and Protection Area, FM Global Engineering and Research, Norwood, MA 02062*
[3]*Chemical Sciences and Engineering Division, Argonne National Laboratory, Argonne, IL 60439*

ABSTRACT: An updated H$_2$/O$_2$ kinetic model based on that of Li et al. (*Int J Chem Kinet* 36, 2004, 566–575) is presented and tested against a wide range of combustion targets. The primary motivations of the model revision are to incorporate recent improvements in rate constant treatment and resolve discrepancies between experimental data and predictions using recently published kinetic models in dilute, high-pressure flames.

Attempts are made to identify major remaining sources of uncertainties, in both the reaction rate parameters and the assumptions of the kinetic model, affecting predictions of relevant combustion behavior. With regard to model parameters, present uncertainties in the temperature and pressure dependence of rate constants for HO$_2$ formation and consumption reactions are demonstrated to substantially affect predictive capabilities at high-pressure, low-temperature conditions. With regard to model assumptions, calculations are performed to investigate several reactions/processes that have not received much attention previously. Results from ab initio calculations and modeling studies imply that inclusion of H + HO$_2$ = H$_2$O + O in the kinetic model might be warranted, though further studies are necessary to ascertain its role in combustion modeling. In addition, it appears that characterization of nonlinear bath-gas mixture rule behavior for H + O$_2$(+ M) = HO$_2$(+ M) in multicomponent bath gases might be necessary to predict high-pressure flame speeds within ∼15%.

The updated model is tested against all of the previous validation targets considered by Li et al. as well as new targets from a number of recent studies. Special attention is devoted to establishing a context for evaluating model performance against experimental data by careful consideration of uncertainties in measurements, initial conditions, and physical model

assumptions. For example, ignition delay times in shock tubes are shown to be sensitive to potential impurity effects, which have been suggested to accelerate early radical pool growth in shock tube speciation studies. In addition, speciation predictions in burner-stabilized flames are found to be more sensitive to uncertainties in experimental boundary conditions than to uncertainties in kinetics and transport. Predictions using the present model adequately reproduce previous validation targets and show substantially improved agreement against recent high-pressure flame speed and shock tube speciation measurements. Comparisons of predictions of several other kinetic models with the experimental data for nearly the entire validation set used here are also provided in the Supporting Information. © 2011 Wiley Periodicals, Inc. Int J Chem Kinet 44: 444–474, 2012

INTRODUCTION

The H$_2$/O$_2$ reaction system is a fundamental topic in combustion science that has historically received significant attention due to both its rich kinetic behavior and its importance to a variety of applications in energy conversion. Since H$_2$ and the intermediate oxidation species are also dominant intermediate species in the oxidation of all hydrocarbon and oxygenated fuels, the H$_2$/O$_2$ mechanism not only forms an essential subset of any hydrocarbon or oxygenate oxidation mechanism [1] but also contains a number of reactions whose rate constants are among the most sensitive for combustion predictions for all hydrocarbon and oxygenate fuels. Recently, there has also been considerable interest in H$_2$ (either pure or mixed with predominantly CO, CO$_2$, and H$_2$O) as a fuel itself or as a main component of synthetic gas or "syngas" from coal or biomass gasification. Integrated gasification combined cycle processes involve gasifying a solid hydrocarbon feedstock to produce syngas that is typically combusted in gas turbine engines. Such processes offer promise for efficient, low-emission power generation with increased potential for carbon capture and storage compared to conventional coal technologies. Lean, premixed combustion of syngas with dilution allows for reduction of the peak flame temperature to lower NO$_x$ emissions. However, fully premixed combustion has not been utilized in commercial syngas applications due to a number of technical challenges associated with the approach; these include blowout, flashback, autoignition, and combustion dynamics [2]. As a result of interest in and difficulties associated with gas turbine syngas combustion, robust fluid dynamic as well as chemical kinetic modeling tools are sought that are thoroughly validated against experiments spanning a wide range of operating conditions. The ultimate goal of these modeling efforts is to achieve accurate predictive behavior of dynamic combustor features necessary for reliable operation [3].

There is general confidence in the combustion community in the H$_2$ mechanism and a perception among some that all H$_2$ oxidation models are essentially the same in terms of their prediction characteristics. One might conclude (mistakenly) that kinetic uncertainties are sufficiently small as to now be of little importance, though it appears likely that the system is least understood at the conditions most relevant to applications. Like most applications, syngas combustion in gas turbines employs higher pressures (10–30 atm) to improve efficiencies and lower flame temperatures to reduce NO$_x$ emissions (less than ∼1800 K). The higher pressures, lower flame temperatures, and high collision efficiencies of common syngas diluents such as CO$_2$ and H$_2$O produce a kinetic regime that is largely controlled by HO$_2$ and H$_2$O$_2$ pathways, which are considerably less characterized than the branching reactions that dominate many of the systems previously used as validation targets for H$_2$ mechanisms. A number of studies (e.g., [4–11]) have recently emerged that present experimental data at high-pressure and/or low-temperature conditions. Comparisons of these experimental data and model predictions using recently published kinetic models [12–18] reveal noteworthy disagreement, particularly for high-pressure and/or dilute flames [6–9]. Since the publication of many of these studies [4–11], Hong et al. [19] published an updated H$_2$/O$_2$ model on the basis of their recent shock tube measurements to determine improved rate constants for several reactions. The model of Hong et al. [19] shows significant improvements against homogeneous targets, particularly for recent shock tube speciation and ignition delay time data. However, predictions using the model of Hong et al. [19] bring no further resolution to discrepancies observed for high-pressure and/or dilute flame speeds [4–9] (e.g., see Figs. S8–S10 in the Supporting Information). Concurrent work leading to the updated model presented here achieves equal or better agreement with homogeneous validation targets as well as significant improvements in predicting high-pressure and/or dilute flame targets.

There were three critical aspects of the present work that led to this updated model. First, we updated our previous H$_2$/O$_2$ model [12] to incorporate recent

improvements in rate constant and transport treatment from fundamental studies as well as to improve agreement with flame speed measurements at high-pressure, dilute flame conditions, and speciation measurements in shock tubes. Second, we identified major sources of uncertainties in the model that result in uncertainties in predictions of relevant combustion behavior. Calculations were performed in several instances to investigate the effects of reactions/processes that have not received much attention previously, including the pressure dependence of $H + O_2 = OH + O$ (R1), temperature dependence of $H + HO_2$ reaction channels, significance of $O + OH + M = HO_2 + M$ (X6), and nonlinear bath-gas mixture rules for $H + O_2(+M) = HO_2(+M)$ (R9) in multicomponent bath gases. (See Tables I and III later in this paper for a complete list of reactions treated in this study.) As shown below, uncertainties in model predictions are not exclusively attributable to uncertainties in model parameters; prediction uncertainties are also attributable to uncertainties in the mechanistic description of the model. For example, our studies imply that the inclusion of $H + HO_2 = H_2O + O$ (X1) (which is only included in some kinetic models [13–15,17,18]) and treatment of nonlinear bath-gas mixture rules for (R9) (which is not included in any H_2 kinetic model) may be necessary to achieving accurate predictions of high-pressure, low-temperature combustion behavior. Third and finally, we tested the performance of the updated model against experimental data for a wide range of reaction conditions and observables—including all of the validation targets used for our previous model [12] as well as new targets from a number of recent studies. The effect of uncertainties in measurements, initial conditions, and physical model assumptions surrounding the experimentally determined values themselves on interpretation of the experimental data was investigated to provide a proper context for assessing model performance against validation targets. In particular, we found that hydrocarbon impurities and other nonidealities in shock tubes and boundary condition uncertainties in burner-stabilized flames can have significant impacts on interpretation of measurements for ignition delay times and flame speciation, respectively.

MODEL FORMULATION APPROACH

The present model is formulated in a manner that balances consistency with data for both elementary reactions and combustion behavior. There have been numerous recent noteworthy improvements in the characterization of rate constants for key reactions in the H_2/O_2 system (discussed below) that warrant reconsid-

eration of rate constant treatment in H_2 kinetic modeling. Theoretical calculations were employed in several instances in the present study to provide further insight into processes or reactions where improved fundamental characterization was necessary.

However, a kinetic model constructed solely from knowledge of isolated, elementary reactions cannot be expected to yield the level of prediction accuracies typically desired for behavior involving the entire system of reactions. As an example, our previous work has shown the highest accuracies typically achievable for rate constant determination under "favorable circumstances" ($\sim$10% [20]) for every reaction rate constant at every temperature and pressure will yield still $\sim$30% uncertainties in predicted high-pressure flame speeds—far beyond what is usually considered good agreement for flame speeds [9]. Present rate constant uncertainties clearly are considerably higher. Therefore, the best choice of rate parameters for some reactions is relatively arbitrary when considering only fundamental knowledge of the particular reaction in isolation, but the choice of rate parameters for the reaction can have a substantial impact on predictions of combustion behavior. For example, while rate constants for $HO_2 + HO_2 = H_2O_2 + O_2$ (R14) determined from two different studies from the same laboratory [21,22] employing similar techniques are different by a factor of three, as discussed below, they yield flame speed predictions at some conditions that are different by 10–20%. Under such circumstances, the rate constant used in the present model was chosen to yield better agreement with combustion targets. This type of approach is akin to inclusion of the coupled constraints on several rate parameters imposed by the combustion targets with the motivation that similar cancellation of errors might occur across a wider range of conditions. We emphasize here that validation is a necessary but not sufficient condition for model accuracy across a range of conditions, though a model that is validated against a more diverse set of experimental data should yield better predictions over a wider range of conditions. However, to facilitate further improvements in kinetic modeling, we have attempted to identify the major remaining sources of uncertainties, in both the parameters and the assumptions of the kinetic model, affecting predictions of relevant combustion behavior. Given the already broad scope of the current work, we have decided not to perform a global mathematical optimization in the present paper. However, we are developing a new optimization approach that balances consistency with raw data from both elementary reaction and combustion experiments as well as ab initio calculations, much as we have attempted to do here, in a more mathematically formal manner [23].

Given the considerable uncertainties that remain in the temperature, pressure, and bath gas dependence of rate constants, we have decided to formulate our kinetic model in a manner compatible with the standard CHEMKIN format subject to its current limitations in the representation of rate constant forms (e.g., limitations regarding unimolecular/recombination reactions detailed in the Appendix). However, throughout the text we make note of situations where better rate constant representations would be worthwhile.

More accurate treatment of transport can be achieved through the use of the updated transport database compiled by Wang and coworkers [24]. The use of the updated transport database requires the use of modified interpreters and subroutines also provided by Wang and coworkers [24]. Predictions of the present model are shown with the updated transport treatment [24], and we recommend its use in conjunction with the present kinetic model. However, we note that similar agreement with the present validation set is achieved using conventional Lennard–Jones transport compatible with the CHEMKIN format.

UPDATED H₂/O₂ KINETIC MODEL AND ASSESSMENT OF MAJOR UNCERTAINTIES

The present model incorporates the 19-reaction scheme evaluated in our previous modeling work [12]. Rate constants for a number of reactions were reviewed during the construction of the present model. The present reaction model and relevant thermochemistry are provided in Tables I and II, respectively. A list of neglected reactions (discussed in more detail below) for which rate constants are available is provided in Table III, along with notes regarding their impact on predictions. In the following paragraphs, we discuss the particular rate constants used in the present model and remaining uncertainties in elementary processes that lead to substantial uncertainties in predictions of relevant combustion behavior. To provide a context for the importance of the reactions considered in the present model update as related to its ability to predict combustion behavior, sensitivity coefficients are shown in Fig. 1 for a small, representative set of conditions. In addition, conditions in the present validation set for which rate constants are sensitive are outlined for many of the reactions discussed below.

H + O₂ (+M)=HO₂ (+M)   (R9)

The recombination reaction (R9) competes with the branching reaction (R1) for H atoms—largely governing the overall branching ratio in combustion systems and determining the second explosion limit in homo-
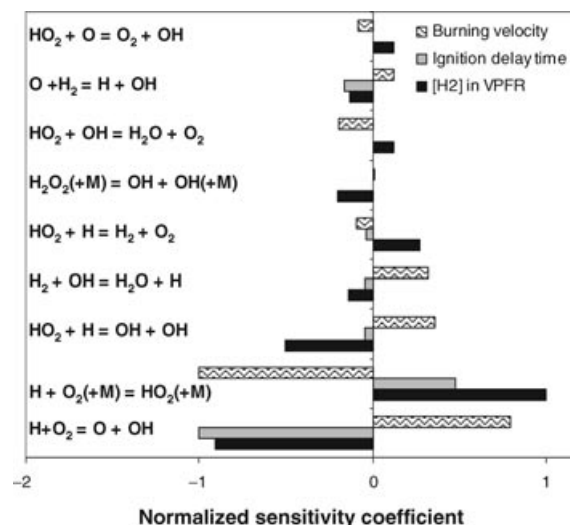
Figure 1 Normalized sensitivity coefficients of observables to A-factors of reactions for selected representative cases: flame burning velocity [9], ignition delay time [10], and fuel consumption in a flow reactor [47]. Sensitivity coefficients are normalized by the maximum sensitivity coefficient for each case. Analysis was performed for an H₂/O₂/He flame of equivalence ratio 0.70 at 10 atm of flame temperature near 1400 K [9]; an H₂/O₂/Ar mixture composed of H₂ = 4%, O₂ = 2%, and Ar balance at 1100 K and 3.5 atm [10]; and a H₂/O₂/N₂ mixture composed of H₂ = 1.01%, O₂ = 0.52%, and N₂ balance at 934 K and 3.4 atm [47]. The sensitivity coefficient for the flow reactor case is taken at the time when 50% H₂ has been consumed.

geneous H₂/O₂ systems. Consequently, reactions (R9) and (R1) are among the most important reactions in combustion chemistry, as illustrated by their high sensitivity coefficients for a variety of systems, e.g., Fig. 1. As such, there is an enormous body of work devoted to both of these reactions. The rate constant expression for k_9 used in the present model (see Table I) is largely based on recent assessment of experimental data in the low-pressure limit by Michael et al. [25] and recent studies in the falloff regime [26–32].

In a similar manner to our previous model [12], we provide one complete expression for k_0, k_∞, F_c, and ε_i for mixtures where N₂ is the primary bath gas and another expression for mixtures where Ar or He is the primary bath gas. The present model retains the low-pressure limit rate constant and third-body efficiencies used in Li et al. [12], which were based on the assessment of Michael et al. [25], for all bath gases except H₂O. The third-body efficiency for H₂O was increased by a factor of 1.3 from that used in our previous model [12] for two reasons: (1) to improve consistency of the complete expression used here with the high-temperature experimental data of Bates et al. [27] and (2) to improve agreement with burning rates of

Table I H_2/O_2 Reaction Model

		A	n	E_a		Reference
(1)	$H + O_2 = O + OH$	1.04E+14	0.00	1.531E+04	*	[42]
(2)	$O + H_2 = H + OH$ Duplicate	3.82E+12	0.00	7.948E+03	*	[20]
	Duplicate	8.79E+14	0.00	1.917E+04		
(3)	$H_2 + OH = H_2O + H$	2.16E+08	1.51	3.430E+03		[147]
(4)	$OH + OH = O + H_2O$	3.34E+04	2.42	−1.930E+03	*	[20]
(5)	$H_2 + M = H + H + M$	4.58E+19	−1.40	1.040E+05		[81]
	$\varepsilon_{H2} = 2.5, \varepsilon_{H2O} = 12.0, \varepsilon_{CO} = 1.9, \varepsilon_{CO2} = 3.8, \varepsilon_{Ar} = 0.0, \varepsilon_{He} = 0.0$					[12]
	$H_2 + Ar = H + H + Ar$	5.84E+18	−1.10	1.040E+05		[81]
	$H_2 + He = H + H + He$	5.84E+18	−1.10	1.040E+05		[12]
(6)	$O + O + M = O_2 + M$	6.16E+15	−0.50	0.000E+00		[81]
	$\varepsilon_{H2} = 2.5, \varepsilon_{H2O} = 12.0, \varepsilon_{CO} = 1.9, \varepsilon_{CO2} = 3.8, \varepsilon_{Ar} = 0.0, \varepsilon_{He} = 0.0$					[12]
	$O + O + Ar = O_2 + Ar$	1.89E+13	0.00	−1.790E+03		[81]
	$O + O + He = O_2 + He$	1.89E+13	0.00	−1.790E+03		[12]
(7)	$O + H + M = OH + M$	4.71E+18	−1.00	0.000E+00		[81]
	$\varepsilon_{H2} = 2.5, \varepsilon_{H2O} = 12.0, \varepsilon_{CO} = 1.9, \varepsilon_{CO2} = 3.8, \varepsilon_{Ar} = 0.75, \varepsilon_{He} = 0.75$					[12]
(8)	$H_2O + M = H + OH + M$	6.06E+27	−3.32	1.208E+05	*	[82]
	$\varepsilon_{H2} = 3.0, \varepsilon_{H2O} = 0.0, \varepsilon_{CO} = 1.9, \varepsilon_{CO2} = 3.8, \varepsilon_{O2} = 1.5, \varepsilon_{N2} = 2.0, \varepsilon_{He} = 1.1$					See text
	$H_2O + H_2O = H + OH + H_2O$	1.01E+26	−2.44	1.202E+05		[82]
(9)	$H + O_2 (+M) = HO_2 (+M)^a$ k_∞	4.65E+12	0.44	0.000E+00	*	[26]
	k_0	6.37E+20	−1.72	5.250E+02		[25], M = N_2
	$F_c = 0.5, T^{***} = 1.0E–30, T^* = 1.0E+30$				*	[32]
	$\varepsilon_{H2} = 2.0, \varepsilon_{H2O} = 14.0, \varepsilon_{CO} = 1.9, \varepsilon_{CO2} = 3.8, \varepsilon_{O2} = 0.78, \varepsilon_{Ar} = 0.67, \varepsilon_{He} = 0.8$				*	See text
	$H + O_2 (+M) = HO_2 (+M)^b$ k_∞	4.65E+12	0.44	0.000E+00	*	[26]
	k_0	9.04E+19	−1.50	4.920E+02		[25], M = Ar or He
	$F_c = 0.5, T^{***} = 1.0E–30, T^* = 1.0E+30$					[32]
	$\varepsilon_{H2} = 3.0, \varepsilon_{H2O} = 21.0, \varepsilon_{CO} = 2.7, \varepsilon_{CO2} = 5.4, \varepsilon_{O2} = 1.1, \varepsilon_{He} = 1.2, \varepsilon_{N2} = 1.5$				*	See text
(10)	$HO_2 + H = H_2 + O_2$	2.75E+06	2.09	−1.451E+03	*	[53] × 0.75
(11)	$HO_2 + H = OH + OH$	7.08E+13	0.00	2.950E+02		[12]
(12)	$HO_2 + O = O_2 + OH$	2.85E+10	1.00	−7.239E+02	*	[90] × 0.6
(13)	$HO_2 + OH = H_2O + O_2$	2.89E+13	0.00	−4.970E+02		[52]
(14)	$HO_2 + HO_2 = H_2O_2 + O_2$ Duplicate	4.20E+14	0.00	1.200E+04		[21]
	$HO_2 + HO_2 = H_2O_2 + O_2$ Duplicate	1.30E+11	0.00	−1.630E+03		
(15)	$H_2O_2 (+M) = OH + OH (+M)$ k_∞	2.00E+12	0.90	4.875E+04	*	[94]
	k_0	2.49E+24	−2.30	4.875E+04	*	[94]
	$F_c = 0.42, T^{***} = 1.0E–30, T^* = 1.0E+30$				*	[94]
	$\varepsilon_{H2O} = 7.5, \varepsilon_{H2O2} = 7.7, \varepsilon_{CO2} = 1.6, \varepsilon_{O2} = 1.2, \varepsilon_{N2} = 1.5, \varepsilon_{He} = 0.65$				*	[94]
	$\varepsilon_{H2} = 3.7, \varepsilon_{CO} = 2.8$					See text
(16)	$H_2O_2 + H = H_2O + OH$	2.41E+13	0.00	3.970E+03		[81]
(17)	$H_2O_2 + H = HO_2 + H_2$	4.82E+13	0.00	7.950E+03		[81]
(18)	$H_2O_2 + O = OH + HO_2$	9.55E+06	2.00	3.970E+03		[81]
(19)	$H_2O_2 + OH = HO_2 + H_2O$ Duplicate	1.74E+12	0.00	3.180E+02	*	[87]
	Duplicate	7.59E+13	0.00	7.270E+03		

Units are cm^3 mol s cal K; $k = AT^n \exp(-E_a/RT)$.

*Indicates the reaction has been revised from that used in Li et al. [12].

[a]Recommended for use with mixtures where N_2 is the primary bath gas.

[b]Recommended for use with mixtures where Ar or He is the primary bath gas.

high-pressure laminar premixed flames, which are highly sensitive to the third-body efficiency of H_2O at high temperatures near the postflame zone. When the data of Bates et al. [27] are interpreted using a cen-

tering factor of 0.5 used here (instead of a centering factor of 0.8 used in Bates et al. [27] and Michael et al. [25]), the derived low-pressure limit rate constant is higher by a factor of 1.3 (see Fig. 2a).

Table II ΔH_f (298.15), S (298.15), and C$_p$ (T) for Species Considered in the H$_2$/O$_2$ Reaction Mechanism

Species	ΔH_f (298.15)	S(298.15)	C_p (300)	C_p (500)	C_p (800)	C_p (1000)	C_p (1500)	C_p (2000)
H	52.10	27.39	4.97	4.97	4.97	4.97	4.97	4.97
O	59.56	38.47	5.23	5.08	5.02	5.00	4.98	4.98
OH	8.91	43.91	7.16	7.05	7.15	7.34	7.87	8.28
H$_2$	0.00	31.21	6.90	7.00	7.07	7.21	7.73	8.18
O$_2$	0.00	49.01	7.01	7.44	8.07	8.35	8.72	9.03
H$_2$O	−57.80	45.10	8.00	8.45	9.22	9.87	11.26	12.22
HO$_2$	3.00	54.76	8.35	9.47	10.77	11.38	12.48	13.32
H$_2$O$_2$	−32.53	55.66	10.42	12.35	14.29	15.21	16.85	17.88
N$_2$	0.00	45.77	6.95	7.08	7.50	7.83	8.32	8.60
Ar	0.00	36.98	4.97	4.97	4.97	4.97	4.97	4.97
He	0.00	30.12	4.97	4.97	4.97	4.97	4.97	4.97

Units are cal mol^{-1} K^{-1} for S and C_p, and kcal mol^{-1} for ΔH_f.
Thermochemical parameters used here are the same as used in Li et al. [12].

Table III   Neglected Reactions in the H$_2$/O$_2$ Reaction Model (for Which Rate Constants Are Available)

			A	n	E_a	Reference
(X1)	HO$_2$ + H = H$_2$O + O	Either	2.90E+08	1.55	−1.601E+02	[48]
		Or	5.90E+12	0.81	7.700E+03	[54]
		Or		see Fig. 8		Present study
(X2)	HO$_2$ + H + M = H$_2$O$_2$ + M		Negligible			[48]
(X3)	OH + OH = H$_2$ + O$_2$		2.00E+11	0.51	5.050E+04	[54]
(X4)	H$_2$O + O = H$_2$ + O$_2$		1 .07E+10	0.97	6.870E+04	[54]
(X5)	H$_2$O$_2$ + O = H$_2$O + O$_2$		8.43E+11	0.00	3.970E+03	[20] (upper limit)
(X6)	O + OH + M = HO$_2$ + M	Either	1.00E+15	0.00	0.000E+00	[98][a]
		Or	1.00E+17	0.00	1.000E+00	[1]

Units are cm^3 mol s cal K; $k = AT^n \exp(-E_a/RT)$.
[a] Supported by the present calculations.

A number of recent studies of (R9) in the falloff regime have motivated us to update the falloff treatment of this reaction. The present expression uses the high-pressure limit value proposed by Troe [26] based on ab initio calculations [31]. The expression is consistent with more recent calculations from Troe and Ushakov [30] at combustion-relevant temperatures, calculations from Sellevåg et al. [29], high-pressure limit measurements of Cobos et al. [33] at 298 K, high-pressure limit measurements in supercritical H$_2$O of Janik et al. [34] from 298 to 623 K, and extrapolations from the intermediate falloff measurements of Fernandes et al. [32] (with the use of a centering factor of 0.5) from 300 to 900 K. It should be noted that all of these studies suggest a high-pressure limit rate constant that is a factor of three higher than that calculated by Bates et al. [27] using hindered-Gorin RRKM (Rice–Ramsperger–Kassel–Marcus) theory. A temperature-independent centering factor of 0.5 is used to represent the falloff behavior of all bath gases in the present expression. This centering factor can be used to properly

describe measurements of (R9) for temperatures from 300–900 K in Ar, N$_2$, and He [28,32].

Rate constants calculated from the present expression are compared with experimental data in intermediate falloff from Bates et al. [27] and Fernandes et al. [32] in Fig. 2. The present expression is consistent with measurements of Bates et al. [27] at 1200 K in Ar, N$_2$, and H$_2$O except at the highest pressures in Ar. Furthermore, both the expression recommended for use in mixtures with N$_2$ as the primary bath gas and the expression for mixtures with Ar or He as the primary bath gas in the present model reproduce the measured rate constant for H$_2$O as the bath gas well. None of the recently proposed expressions [20,26–32] reproduces the observed pressure dependence of the rate constant in Ar. Reproducing the data within error bounds for Ar using high-pressure limit values indicated by recent studies [29,32–34] requires a low-pressure limit rate constant higher by 50% and a falloff centering factor of 0.2. A falloff centering factor of 0.2 would appear to be inconsistent with theoretical predictions and

measurements by Fernandes et al. [32] from 300–900 K in Ar that are well represented by a temperature-independent centering factor of 0.5 over a wide range of pressures. The present rate constant expression reasonably reproduces measurements in the intermediate falloff regime from 300–900 K in Ar, N_2, and He from Fernandes et al. [32], though their data set might support a low-pressure limit for He that is lower than the assessment of Michael et al. [25]. The present expression for N_2 shows substantial improvements compared to that used in our previous model [12], where the previous expression overpredicts the observed rate constant in intermediate falloff. Overall, the present expression represents the experimental data in the intermediate falloff regime [27,32] with a standard deviation of 33%.
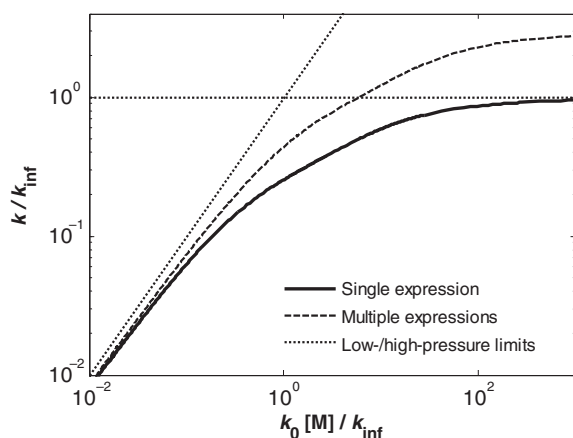
Given the complexity of unimolecular reactions in terms of their temperature, pressure, and bath-gas dependences, the persistent scatter in the low-pressure limit data, scarcity of data at combustion temperatures, and semiempirical nature of present theoretical calculation strategies, there continues to be a great deal of uncertainty in the rate constant even in single-component bath gases despite the large amount of attention devoted to reaction (R9). Calculation of rate constants for multicomponent bath gases from rate constants developed for single-component bath gases requires a bath-gas mixture rule, which introduces additional uncertainties. The potential for error is especially large in the falloff regime, where there is at present a lack of studies devoted to fundamental understanding and testing of mixture rules. For example, Fig. 3 compares two expressions presently available in CHEMKIN software (described in the Appendix) for a bath gas composed of 33.3% Ar, 33.3% Ar_{f1}, and 33.3% Ar_{f2}. The fictional species, Ar_{f1} and Ar_{f2}, are given the same thermodynamic and kinetic parameters as Ar. The "single-expression" treatment used here and in the models of [12,13,16,17] is compared to the "multiple-expression" treatment used in the models of [14,15,19]. In this particular example, the single-expression treatment yields identical results to the case where the bath gas is 100% Ar. However, the multiple-expression treatment overpredicts the rate constant in falloff by up to a factor equal to the number of separate expressions for (R9). Such a result can be attributed to the fact that the different expressions in the multiple-expression treatment are assumed to be independent. Therefore, it does not account for the fact that the concentration of excited adduct, through which (R9) proceeds for each collision partner, is reduced by stabilization by all collision partners in high-pressure falloff. A recently proposed mixture rule [35] yields substantial improvements, particularly in terms of re-
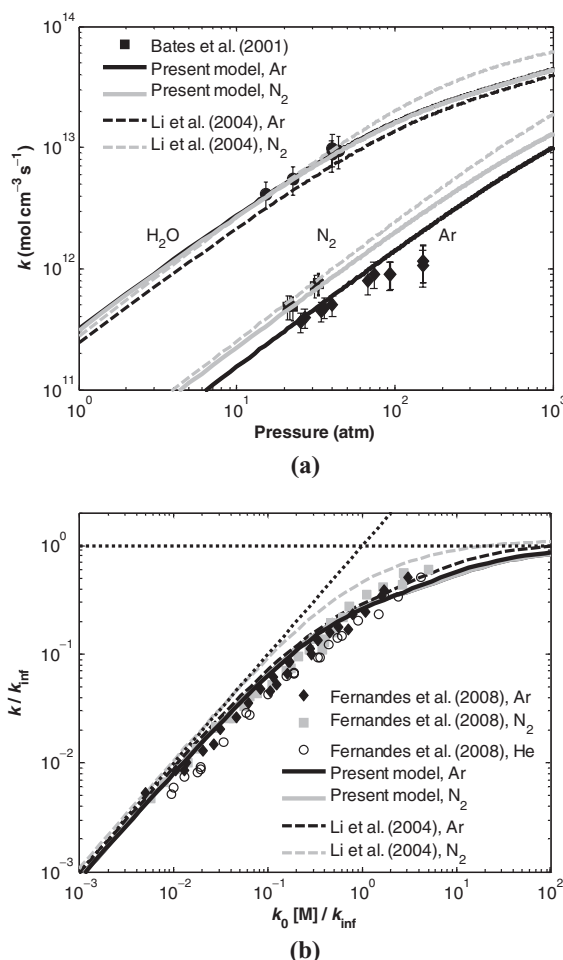
Figure 2   Rate constants for $H + O_2(+M) = HO_2(+M)$ (R9) in intermediate falloff. Symbols represent experimental data for k_9 measured in (a) Ar, N_2, and H_2O at 1200 K by Bates et al. [27] and (b) Ar, N_2, and He from 300 to 900 K by Fernandes et al. [32]; solid lines the present model; dashed lines the model of Li et al. [12]; dotted lines: low- and high-pressure limit rate constants used in the present model. Black (gray) lines denote the rate constant expressions for use in mixtures where Ar (N_2) is the primary bath gas (see the text).

producing the high-pressure limit, though the expression is not yet available as an option in CHEMKIN software.
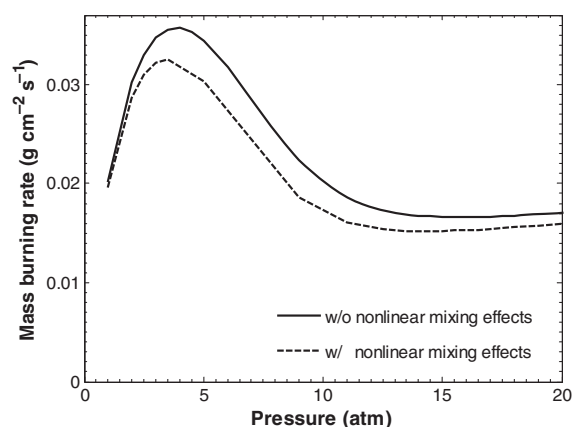
While the above-mentioned mixture rules differ in terms of their description of the falloff regime, all of them assume a linear mixture rule in the low-pressure limit. However, previous theoretical studies have indicated deviations from the linear mixture rule in the low-pressure limit if one of the bath-gas components is a weak collider with an average energy transferred per collision, $\langle \Delta E \rangle$, that differs from the other colliders in the mixture [36,37]. The nonlinear behavior can be attributed to the fact that the rovibrational energy

Figure 3 Demonstration of two standard treatments for unimolecular reaction rate constants for H + O$_2$(+M) = HO$_2$(+M) for a bath gas composed of 33.3% Ar, 33.3% Ar$_{f1}$, and 33.3% Ar$_{f2}$. The fictional species, Ar$_{f1}$ and Ar$_{f2}$, are given the same thermodynamic and kinetic parameters as Ar. See the text for a description of the two treatments.

Figure 4 Laminar flame mass burning rates in H$_2$/O$_2$/He mixtures of equivalence ratio 0.3 and He dilution such that the adiabatic flame temperature is near 1400 K. Solid lines represent the present model; dashed lines a modified version of the present model where k_9 is adjusted to simulate nonlinear mixture behavior.

distribution of the reactant in bath gases composed of colliders with varied energy transferred per collision, $\langle\Delta E\rangle$, will vary with composition. Master equation solutions by Dove et al. [37] show that the rate constant in a multicomponent bath gas is always higher than that predicted by the linear mixture rule. Analytical solutions of the master equation by Troe [36] indicate that deviations are higher when components have greater differences in $\langle\Delta E\rangle$ values and the stronger collider is present in mole fractions of 5–10%. Substitution of representative values for $\langle\Delta E\rangle$ of common bath gases into the analytical solutions yields deviations from the linear mixture rule of up to ∼10% [36]. While deviations of that magnitude are likely to be below the detection limit of elementary kinetic experiments, the high sensitivity of kinetic model predictions to k_9 and disparity of $\langle\Delta E\rangle$ values among bath gas components in high-pressure, dilute flames suggest that nonlinear mixture behavior may be an important factor to consider.

For example, in the flame conditions shown in Fig. 4, the mole fraction of H$_2$O (considered to be a much stronger collider than typical diluents such as N$_2$, Ar, and He [25,32]) increases as the extent of reaction increases throughout the flame. Consumption pathway analyses indicate that peak H consumption through (R9) occurs near the postflame zone where the H$_2$O mole fraction is 5–10%—the mole fraction range of the stronger collider where deviations from the linear mixture rule were found to be highest [36], as discussed above. Figure 4 compares flame predictions with and without nonlinear mixing effects (the former are sim-

ulated by a 10% increase in the A-factor). Differences of approximately 15% are observed.

Given the present limited understanding of mixture behavior as well as $\langle\Delta E\rangle$ values for relevant bath gases, the extent of nonlinear deviations in k_9 is unclear. At present, we have not attempted to include these effects in our kinetic model. However, until further advances are made on collisional energy transfer properties, it appears that uncertainties of up to ∼20% should be expected due to the fundamental laws of the kinetic model alone (not including parameter uncertainties). In fact, rate constants for unimolecular and recombination reactions calculated from fitting formulas, such as the conventional Troe formula [38–40] used here, have also been shown to differ from the rate constants from the master equation solutions, which were used for the fitting, by up to ∼20% [41]. Furthermore, experimental and theoretical studies on k_9 suggest that the rate constant exhibits asymmetric broadening in falloff [32]. More generally, however, it appears that achieving accuracies typically expected for flame speeds (∼20% or below) with the high sensitivities encountered in high-pressure flames may require consideration of a number of processes that are generally considered to be negligible.

H + O$_2$=OH + O   (R1)

As mentioned above, the branching reaction (R1) is among the most important reactions in combustion chemistry for a variety of fuels. The present model uses the rate constant for (R1) recently proposed by Hong et al. [42] (see Fig. 5). Their expression is based on
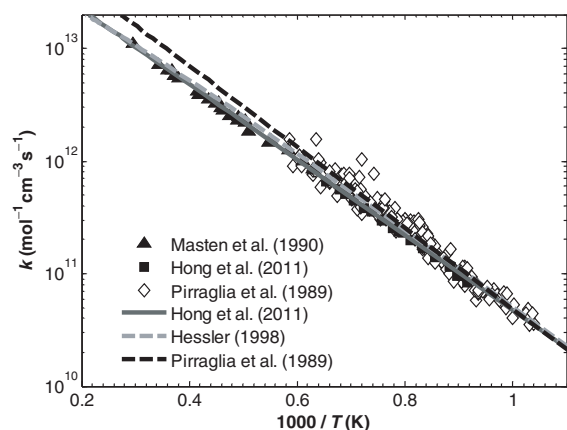
Figure 5 Rate constants for H + O₂ = OH + O (R1). Symbols represent experimental data [42–44], and lines represent proposed rate constant expressions [42,44,45] commonly used in modeling as indicated in the legend. The model of Li et al. [12] uses the expression from Hessler [45]. The present model uses the expression from Hong et al. [42].

a two-parameter Arrhenius fit to values for k_1 derived from H_2O absorption measurements in shock-heated $H_2/O_2/Ar$ mixtures over the temperature range from 1100 to 1530 K and those derived from OH absorption measurements from 1450 to 3370 K by Masten et al. [43], representing the two data sets with a standard deviation of 10% over the full temperature range [42]. The two sets of measurements [42,43] agree well over the overlapping temperature range. The experimental data and the proposed rate expression from Hong et al. agree with the experimental data of Pirraglia et al. [44] within experimental scatter. The rate constant used here from Hong et al. [42] is 6–13% lower than the rate constant proposed by Hessler [45] and used in our previous model [12] over the temperature range from 1000 to 3000 K, resulting in better fidelity to the data of Hong et al. [42] from 1100 to 1530 K. To ensure consistency of the rate constant expression proposed by Hong et al. [42] and the other rate constants used in the present model, we compared our predictions against the measured H_2O [42] and OH [43] time histories, from which the k_1 values were originally derived (see Figs. 11 and 12 later in this paper).

Owing to the high sensitivity to the branching ratio between (R1) and (R9), the fact that (R9) undergoes fall off at conditions relevant to combustion applications and the fact that (R1) is a chemically activated reaction that proceeds through the same HO_2 potential surface as (R9) [46], we became concerned with the potential pressure dependence of (R1). However, simple considerations, verified with sample master equation calculations, indicate that k_1 is not noticeably pressure-dependent below 1000 atm. In particular, at energies

high enough for the reaction to proceed, the lifetime of the HO_2 complex is less than 0.1 ps. Meanwhile, at 1000 atm the collision rate is only $\sim 10^{12}$ s^{-1}. Thus, even at 1000 atm, the chemically activated HO_2 complex will dissociate before any collisions with the bath gas take place, in which case there can be no pressure dependence of the kinetics. (It is worth noting that the excited complexes that have sufficient energy to undergo decomposition to OH + O have considerable excess energy and thus decompose more rapidly than those complexes that are responsible for nearly all of the formation of HO_2 through stabilization. Therefore, falloff is observed at much lower pressures for (R9) than for (R1).) This observation supports the traditional treatment, where (R1) and (R9) are considered as independent reactions and (R1) is considered to be in the low-pressure limit.

H + HO₂=Products   (R10, R11, X1)

The H + HO_2 reactions are important consumption pathways of HO_2 and H, particularly at higher pressures, where branching between the different H + HO_2 channels affects the overall branching ratio and contributes to the extended second limit [47], particularly in flow reactor speciation and high-pressure flames (see Fig. 1). As such, the rate constants for these reactions are among the most sensitive in many combustion environments. However, there are relatively few studies of the rate constants for the various channels, particularly at higher temperatures. While there are a number of possible product channels including stabilization to HOOH and H_2OO [48], previous studies have suggested that those responsible for essentially all of the reaction flux are OH + OH (R11), $H_2 + O_2$ (R10), and $H_2O + O$ (X1) [20,48]. The O atom formed in (X1) can be either O(^{3}P) or O(^{1}D) depending on the exact reaction channel [48]—(X1a) or (X1b), respectively. Proposed rate constants for the two major channels, (R10) and (R11), from the various studies discussed below are plotted in Fig. 6.

Baldwin and Walker [49] deduced ratios of rate constants of reactions, $(k_{11} + k_{X1})/(k_1 + k_{14})$ and $k_{10}/(k_1 + k_{14})$ at 773 K from their static reactor experiments [50]. They derived rate constants, $k_{11} + k_{X1}$ and k_{10}, based on rate constants, k_1 and k_{14}, available at the time of their study (1979). Sridharan et al. [51] and Keyser [52] measured rate constants of the three channels ((R10), (R11), (X1)) at 298 K. The results from the two studies are in reasonable agreement. They reveal that the rate constants for the three channels at 298 K are ranked as $k_{X1} < k_{10} < k_{11}$.

Baulch et al. [20] adopted the derived rate constants at 773 K from Baldwin and Walker and further
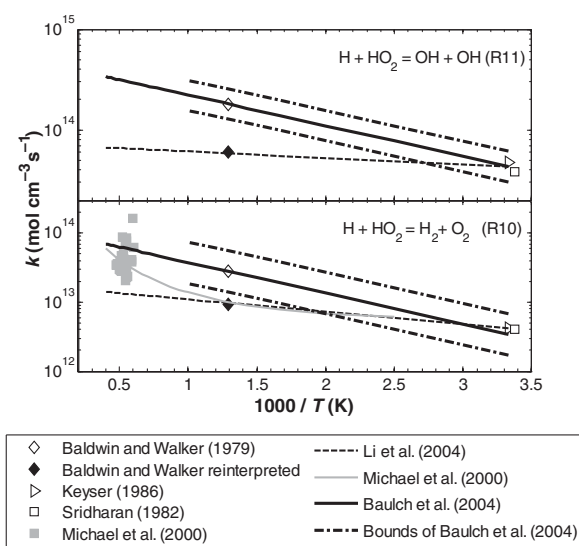
Figure 6 Rate constants for H + HO$_2$ = H$_2$ + O$_2$ (R10) and H + HO$_2$ = OH + OH (R11). Symbols represent experimental data [49–53], and lines represent proposed rate constant expressions [12,20,53] as indicated in the legend. (Note that the experimental datum from Baldwin and Walker [49] shown is the upper plot is actually for $k_{11} + k_{X1}$.) The present model uses the rate constant from Michael et al. [53] with the A-factor scaled by 0.75 for k_{10} and the rate constant from Li et al. [12] for k_{11} (see the text for full description).

assumed $k_{X1} \ll k_{11}$ based on the measurements at 298 K [51,52], which show that $k_{X1} < 0.05\,k_{11}$. They combined the measurements at 298 and 773 K to provide recommended rate constants, k_{10} and k_{11}, which are employed in some H$_2$ kinetic models (e.g., [14]). However, when their deduced ratios are reinterpreted based on rate constants for (R1) and (R14) recommended by Baulch et al. (as well as those used in the present model), the derived rate constants for (R10) and (R11) are more than a factor of three lower than those proposed originally by Baldwin and Walker. In fact, the reinterpreted values for k_{10} and k_{11} are outside the stated uncertainty bounds [20]. As pointed out by Mueller et al. [47] and later by Li et al. [12], it therefore appears that reinterpretation of the experimental data of Baldwin and Walker with improved values for k_1 and k_{14} is necessary to achieve reliable expressions for k_{10} and $k_{11} + k_{X1}$.

More recently, Michael et al. [53], in their study of the reverse reaction (R(−10)), performed conventional transition state theory calculations and shock tube measurements over 1600–2000 K. They proposed a rate constant expression, based on their theoretical results, that agrees well with their high-temperature measurements as well as the low-temperature data and the data from Baldwin and Walker [49], reinterpreted

using the values for k_1 and k_{14} used in the present model. Here, we adopt the rate constant expression proposed by Michael et al. [53] for (R10) while imposing a ∼25% reduction in the A-factor (within present uncertainties) to maintain agreement against the flow reactor speciation data from Mueller et al. [47] in the vicinity of the extended second limit. The resulting expression is in reasonably good agreement with the low-temperature data [51,52], high-temperature data [53], and the reinterpretation of the Baldwin and Walker datum [49] using rate constants employed in the present model.

Studies on the other two product channels, (R11) and (X1), particularly experimental studies, are limited. The rate constant expression used for (R11) in the present model is the same as that used in Li et al. [12]. In a similar manner to that conducted by Mueller et al. [47], the expression was derived from a constant-activation energy Arrhenius fit of the 298 K data [51,50] and 773 K data [49] (reinterpreted using updated values for k_1 and k_{14}—note that k_1 and k_{14} from the present model and Li et al. [12] are within 1% at 773 K). Rate constant calculations using direct variable reaction coordinate transition state theory (assuming no roaming), described below regarding the role of (X1), yield k_{11} values consistent with the expression used here from Li et al. [12] within ∼25% over 300–2000 K.

Measurements for the branching ratio to the H$_2$O + O (X1) channel are limited to atmospheric temperatures, and available theoretical studies result in different conclusions about the importance of (X1) at higher temperatures. Rate constant measurements of the three channels ((R10), (R1), (X1)) at 298 K [51, 52] show that (X1) is responsible for less than 5% of the total flux through H + HO$_2$. The results from the ab initio analysis of the transition states on the lowest triplet H$_2$O$_2$ potential surface by Karkach and Osherov [54] suggest that H + HO$_2$ = H$_2$O + O(^{3}P) (X1a) is responsible for less than 5% of the total flux through H + HO$_2$ for temperatures from 300 to 2000 K. Although results from the theoretical study of Mousavipour and Saheb [48] corroborate the result that (X1a) does not contribute substantially to the total flux, they do suggest that H + HO$_2$ = H$_2$O + O(^{1}D) (X1b), which proceeds through a singlet H$_2$OO surface, could be responsible for up to 15% of the total flux through H + HO$_2$ for temperatures from 300 to 2000 K. Inclusion of reaction (X1) (assuming for simplicity that the O atom produced is in its ground state, ^{3}P) in the present model using the rate constant expression from Mousavipour and Saheb [48] yields substantially faster oxidation rates at flow reactor and high-pressure flame conditions, whereas adopting the rate constant expression from Karkach
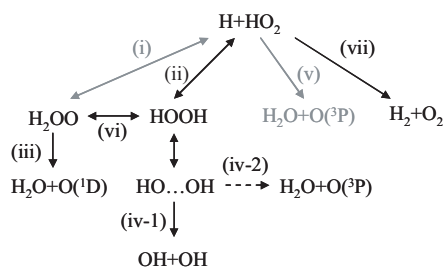
Figure 7 Reaction scheme considered in present calculations for H + HO₂. Black lines denote pathways found to be responsible for significant flux; gray lines denote pathways responsible for insignificant flux; dashed lines denote roaming channels.

and Osherov [54] for (X1) yields negligible effects on predictions for the validation set considered here.

Although the calculations of Mousavipour and Saheb [48] are qualitatively informative, they are not expected to be quantitatively accurate due to limitations in the employed electronic structure and transition state theory methodologies. Thus, to better understand the role of the $H_2O + O$ ((X1a) and (X1b)) channels in the $H + HO_2$ reaction, the following reaction channels (see Fig. 7) were reinvestigated with high level ab initio transition state theory calculations: (i) $H + HO_2 = H_2OO$, (ii) $H + HO_2 = HOOH$, (iii) $H_2OO = H_2O + O(^1D)$, (iv-1) $HOOH = HO\cdots OH = OH + OH$, (iv-2) $HOOH = HO\cdots OH = H_2O + O(^3P)$, (v) $H + HO_2 = H_2O + O(^3P)$, (vi) $H_2OO = HOOH$, and (vii) $H + HO_2 = H_2 + O_2$. The full reaction kinetics was treated within a master equation formalism incorporating either two (HOOH and H_2OO) or three (HOOH, H_2OO, and $HO\cdots OH$) wells. These master equation simulations indicate no significant pressure dependence.

Channels (i)–(iv), which are barrierless, were treated with direct variable reaction coordinate transition state theory [55–58]. The CASPT2/aug-cc-pVDZ method was employed in the direct sampling of the orientational dependence of the interaction energies. One-dimensional corrections for geometry relaxation and limitations in the basis set were incorporated. The geometry relaxation correction was taken as the difference between full optimizations and conserved mode only optimizations for a range of constrained $H\cdots O$ separations. Both optimizations were performed at the CASPT2/aug-cc-pVDZ level. The basis set corrections were obtained from complete basis set estimates based on the extrapolation of CASPT2/cc-pVTZ and CASPT2/cc-pVQZ results evaluated along a qualitative minimum energy path. For channels (i) and (ii), the active space consists of the radical orbitals on H and HO₂. For channel (iii), a larger four electron three orbital (4e,3o) active space was used with an averaging
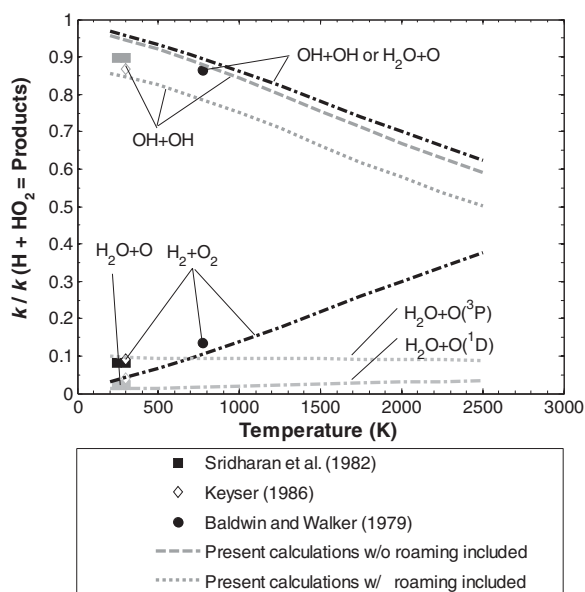
Figure 8 Branching ratios for various channels in the $H + HO_2$ reaction. Dashed lines represent results from present calculations assuming no roaming contribution from (iv); dotted lines represent results from the present calculations with estimations of roaming contribution from (iv); symbols represent experimental data [49, 51, 52]. (Note that calculated rate constants for reaction to $H_2 + O_2$, $OH + OH$ or $H_2O + O$, and $H_2O + O(^1D)$ are not affected by inclusion of roaming from (iv)).

over the five asymptotically degenerate states to properly describe the $O(^1D)$ state. For channel (iv), a (6e,4o) active space with an averaging over four asymptotically degenerate states to properly describe the doubly degenerate OH states. The plane perpendicular to the OO axis was used to separate H_2OO from HOOH in the H + HO₂ addition.

Channels (iv-2) and (v)–(vii), which have well-defined saddle points, were treated with conventional transition state theory [55–58]. The RQCISD(T)/aug-cc-pVTZ method was used to identify and calculate frequencies for the stationary points. Basis set corrections were obtained from the average of complete basis set estimates based on extrapolations of cc-pVQZ,cc-V5Z or aug-cc-pVQZ,aug-cc-pV5Z pairs of calculations. Eckart tunneling corrections were included.

Calculated branching ratios among the main channels are plotted in Fig. 8. Direct formation of $H_2O + O(^3P)$ (v) and stabilization in HOOH or H_2OO are not significant to the total $H + HO_2$ flux. The flux through the H_2OO adduct is predicted to be about 7% of the total flux, essentially independent of temperature. Therefore, the flux through the $H + HO_2$ reaction is dominated by direct formation of $H_2 + O_2$ (vii) and recombination to excited HOOH (ii) followed by

decomposition. The HOOH adduct can isomerize to H_2OO (vi), which decomposes to $H_2O + O(^1D)$ (iii), or decompose directly to $OH + OH$ (iv-1) or $H_2O + O(^3P)$ (iv-2). During the long-range $HO\cdots OH$ interaction of (iv), formation of $H_2O + O(^3P)$ (iv-2) may occur via a radical roaming mechanism. It should be noted that decomposition of HOOH is very fast ($\sim 10^{14}$ s^{-1}), such that statistical predictions of branching between H_2OO (vi) and $HO\cdots OH$ (iv) may be inaccurate. Therefore, reliable calculation of branching characteristics likely necessitates a nonstatistical-based method, e.g., trajectory calculations. Such an endeavor was considered to be outside the scope of the present work.
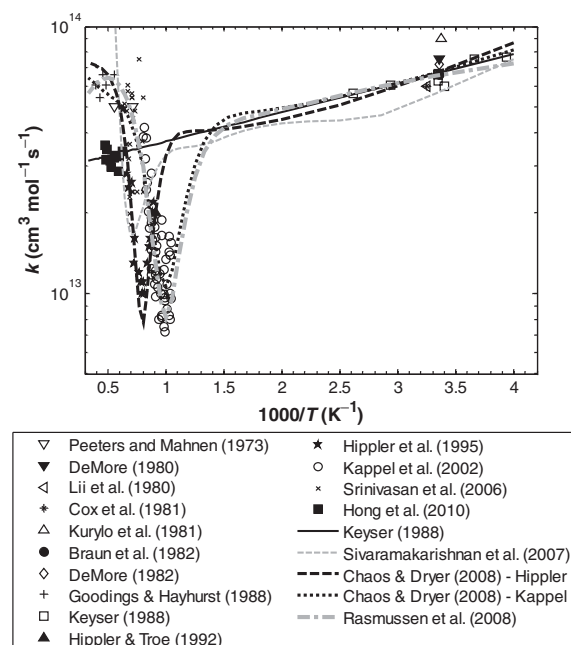
Formation of $H_2O + O(^1D)$, predominantly via $H + HO_2 = HOOH$ (ii) $= H_2OO$ (vi) $= H_2O + O(^1D)$ (iii), is calculated to be responsible for less than 4% of the total $H + HO_2$ flux at temperatures from 300 to 2500 K. Formation of $H_2O + O(^3P)$, predominantly via roaming from $H + HO_2 = HOOH$ (ii) $= HO\cdots OH = H_2O + O(^3P)$ (iv-2), is estimated to account for up to 10% of the total flux. Branching ratios, $k_{X1}/(k_{11} + k_{X1})$ (considering $H_2O + O(^3P)$), of 0, 0.1, and 0.3 were tested in the present model to ascertain their sensitivity on combustion predictions. The branching ratio was varied at fixed $k_{11} + k_{X1}$ since the calculations suggest that both the $OH + OH$ and $H_2O + O$ production channels proceed through (ii). Increasing $k_{X1}/(k_{11} + k_{X1})$ slows overall oxidation, most noticeably in flames and flow reactor speciation at high pressures under near-stoichiometric and rich conditions. The difference between $k_{X1}/(k_{11} + k_{X1}) = 0$ and 0.1 is relatively minimal, though the difference between 0 and 0.3 is rather substantial—altering explosion limit behavior near the extended second limit (observed in flow reactor time evolutions) and flame speeds by up to 30%. At sufficiently rich conditions in which O and OH react predominantly with H_2 (via (R2) and (R3)), both channels (R11) and (X1) yield the sequence: $H + HO_2 + 2H_2 = 2H_2O + 2H$. However, at temperatures below 2000 K, (R3) is substantially faster than (R2) such that the sequence proceeds more quickly and increases the overall oxidation rate, as indicated by the model results. (It should be noted that opposite trends may be observed if O atom is produced in the ^1D rather than ^3P state. The rate constant for $O(^1D) + H_2 = H_2O + H$ is orders of magnitude larger than those for (R2) and (R3).)

Given the potential for nonstatistical behavior of the excited HOOH adduct as well as the complications associated with predicting roaming contributions using present theoretical strategies, the calculated branching ratios presented here are still considered approximate. At present, (X1) is not included in the model, which we consider reasonable given its uncertain role in the $H + HO_2$ reaction. In general, better characterization

of the $H + HO_2$ reaction rate and branching ratios, particularly at combustion temperatures, would be highly beneficial to constraining model predictions in a wide variety of combustion systems. (In this regard, Jasper et al. [59] have begun trajectory calculations on the $H + HO_2$ reaction to evaluate product branching ratios at higher temperatures and better determine the specific role of (X1) in combustion modeling.)

$OH + HO_2 = O_2 + H_2O$ (R13)

Reaction (R13) is an important chain termination reaction that has a rate constant among the most sensitive for lean flame conditions in both H_2 and hydrocarbon systems (e.g., [9]; Fig. 1). A comparison of available experimental data [22,60–73] and proposed rate constant expressions [63, 75–77] is provided in Fig. 9. The reaction has been mostly studied at near atmospheric conditions (e.g., [60–63]), revealing a slight negative temperature dependence. Studies at temperatures above 400 K are considerably fewer (with none below 900 K). Furthermore, available studies at higher temperatures are not entirely consistent, particularly near 1250 K. The derived rate constants for (R13) from measurements by Troe and coworkers [22,69] suggest an uncommon and highly

▽ Peeters and Mahnen (1973)	⋆ Hippler et al. (1995)
▼ DeMore (1980)	○ Kappel et al. (2002)
◁ Lii et al. (1980)	× Srinivasan et al. (2006)
✳ Cox et al. (1981)	■ Hong et al. (2010)
△ Kurylo et al. (1981)	── Keyser (1988)
● Braun et al. (1982)	---- Sivaramakrishnan et al. (2007)
◇ DeMore (1982)	- - - Chaos & Dryer (2008) - Hippler
+ Goodings & Hayhurst (1988)	·········· Chaos & Dryer (2008) - Kappel
□ Keyser (1988)	─·─·─ Rasmussen et al. (2008)
▲ Hippler & Troe (1992)	

Figure 9 Rate constants for $OH + HO_2 = H_2O + O_2$ (R13). Symbols represent experimental data [22,60–73], and lines represent proposed rate constant expressions [63,75–77] as indicated in the legend. The present model uses the rate constant from Keyser [63] for k_{13}.

non-Arrhenius behavior at temperatures between 900 and 1300 K—a deep, narrow "well" in the rate constant with a minimum value nearly an order of magnitude lower than atmospheric and high-temperature values. Hippler et al. [69] observe the rate constant minimum near 1200 K. More recently, Kappel et al. [22] observe the rate constant minimum near 1000 K with a methodology they deem more reliable than that used by Hippler et al. [69]. The two studies [22,69] yield rate constants that differ by a factor of four in the overlapping temperature range (near 1250 K). The data of Srinivasan et al. [70] over the temperature range from 1200 to 1700 K do not exhibit a strong temperature dependence. More recent determinations of (R13) from 1600 to 2200 K by Hong et al. [71] based on rate constant measurements of the reverse reaction reveal a slight negative temperature dependence. Their more direct determinations of k_{13} [71] are a factor of two lower than previous high-temperature determinations from flame studies [72,73]. In addition, their measurements are well described by the rate expression proposed by Keyser [63] based solely on atmospheric temperature measurements. The expression from Keyser [63] assumes a constant activation energy that results in a weak, negative temperature dependence.

Preliminary potential energy surface calculations by Harding and Klippenstein [74] also suggest a weak temperature dependence of k_{13}; they do not support the sharp increase in the rate constant with increasing temperature observed near 1000–1200 K—the *A*-factor required for substantial contributions to k_{13} from such a high-barrier channel would correspond to an unphysical collision frequency.

In addition, rate constant expressions that incorporate the rate constant minimum appear to be incompatible with the other rate constants used in the present model. Substitution of different proposed expressions for (R13) from [75,76] that incorporate the intermediate temperature data that Troe and coworkers deem to be more reliable [22] into the present model yields variations of ignition behavior with an equivalence ratio that are not observed in flow reactor speciation data in the vicinity of the extended second limit [47]. Substitution of different proposed expressions [75–77] that give higher weighting to the other set of intermediate data from Troe and coworkers [69] degrades flame predictions for lean, high-pressure flames. None of the proposed expressions [75–77] that incorporate the intermediate data [22,69], as well as the expression from [78], reproduce the more direct, recent measurements of Hong et al. [71] on the reverse reaction at high temperatures. Given the lack of consistency among experimental data regarding this reaction at intermediate temperatures, lack of theoretical support for the pro-

nounced rate constant minimum, and the incompatibility of the expressions from [75–77] with the set of other rate parameters used in the present model, the present model retains the rate constant expression proposed by Keyser [63], which is used in our previous model [12]. The chosen rate expression agrees well with the low- and high-temperature data and is well within the range of experimental determinations at intermediate temperatures. Nevertheless, independent measurements in the intermediate temperature range would aid in bringing resolution to the discrepancies among experimental, theoretical, and modeling results for the temperature dependence of k_{13}, which is essential to achieving accurate flame predictions for a variety of fuels.

$HO_2 + HO_2 = H_2O_2 + O_2$ (R14)

Reaction (R14) is responsible for HO_2 consumption and H_2O_2 formation under higher pressures and lower temperatures where HO_2 is present in high mole fractions such as in flow reactors and high-pressure flames. The reaction participates in a chain-propagating sequence responsible for thermally driven oxidation kinetics at temperatures above the third explosion limit and below the extended second limit [47]. Similar to the other HO_2 consumption reactions, (R14) has been mostly studied at lower temperatures (e.g., [79,80]). The two primary studies at temperatures above 1000 K are those by Kappel et al. [22], discussed above for (R13), and Hippler et al. [21]. Rate constants for (R14) determined in these two studies differ by a factor of two to three at combustion-relevant temperatures, yielding differences in predicted speciation during the high-pressure H_2 oxidation conditions of Mueller et al. [47] and 10–20% differences in predicted flame speeds at the high-pressure, dilute, lean conditions of Burke et al. [9]. Nevertheless, given the lack of consistency among the studies for k_{13} [22,69] and the dependence of the k_{14} determination on the same data used to derive k_{13} in [22], it is difficult to discern which, if any, k_{14} determination is reliable. At present, we retain the rate constant from Hippler et al. [21] employed in our previous model [12], though we note that further studies on (R14) at combustion temperatures would help constrain uncertainties in predictions of intermediate-temperature speciation and high-pressure, dilute flames.

$H_2O (+M) = H + OH (+M)$ (R8)

The rate constant for (R8), particularly in the reverse direction as a radical–radical recombination reaction, is important to predictions for the flow reactor speciation data from Mueller et al. [47] and flame speeds. Li

et al. [12] and O'Connaire et al. [16] increased the A-factor for (R8) by a factor near two (within the accepted uncertainties at the time) from that recommended by Tsang and Hampson [81] to improve agreement with flame targets. Since the publication of these two models, comparisons of their predictions against more recent experimental flame speed data [8,9] have shown that modification of the rate constant for (R8) is insufficient to predict flame behavior accurately over a wide range of pressure/temperature conditions. In addition, two further studies on the reaction [29,82] have become available recently.

The present model uses rate constant expressions for (R8) in Ar and H$_2$O bath gases as well as third-body efficiencies for other relevant bath gases proposed by Srinivasan and Michael [82]. The expressions are three-parameter Arrhenius expressions based on Troe factorizations; collision efficiencies were chosen to replicate available experimental data for k_8 and k_{-8} that Srinivasan and Michael have determined to be unaffected by secondary reactions. The resulting expressions well replicate experimental data considered in their study [82].

The effect of high-pressure falloff for (R8) was tested by comparing model predictions where (R8) is assumed to be in the low-pressure limit with model predictions where falloff of (R8) is included using the falloff parameters from Sellevåg et al. [29]. Inclusion of falloff for (R8) yielded negligible differences in predictions against the present validation set. As such, (R8) is treated as two expressions (one for Ar and one for H$_2$O) assumed to be in the low-pressure limit as per current CHEMKIN limitations outlined in the Appendix.

OTHER MODIFICATIONS

A number of other rate constants were revised in the present model based on recent determinations and/or recent assessments. The present model employs the rate constant expression for OH + OH = H$_2$O + O (R4) recommended by Baulch et al. [20]. The expression is a three-parameter Arrhenius fit to the data of Bedjanian et al. [83] from ∼230 to 360 K and the data of Wooldridge et al. [84] from 1050 to 2380 K. Baulch et al. [20] note considerable scatter in the measurements on the reverse reaction [85,86], the latter of which served as the basis of the expression that was used in our previous model [12]. However, when the data are combined with thermodynamic data for the reaction, the two studies are in good agreement with that of Wooldridge et al. [84]. Recent indirect measurements by Hong et al. [87] yield k_4 values within 25% of the present expression. Furthermore, predictions us-

ing the present model closely replicate the experimental data [87], from which Hong et al. derive their k_4 values (as shown later in Fig. 13).

Experimental measurements of the rate constant for O + HO$_2$ = O$_2$ + OH (R12) are only available at near-atmospheric temperatures (e.g., [88, 89]), where a weak negative temperature dependence of the rate constant is observed. Most kinetic models and assessments assume no temperature dependence of the rate constant or constant activation energy based on the data from ∼250 to 400 K. Rate constants from ab initio calculations by Fernández-Ramos and Varandas [90] exhibit a weakly negative temperature dependence (consistent with the near-atmospheric temperature data) below ∼400 K, where the reaction proceeds primarily through an addition mechanism. However, the calculated rate constant exhibits a weakly positive temperature dependence at higher temperatures, where the reaction proceeds primarily through H abstraction. The present model employs a three-parameter Arrhenius fit to their calculated rate constant with the A-factor scaled by a factor of 0.6 to match the available measurements at low temperatures. Our previous model employed an expression from Baulch et al. [78] that assumed a constant-temperature extrapolation of the low-temperature data. The expression used here yields similar rate constants near 300 K but higher rate constants by 50% at 1500 K and 80% at 2500 K.

The rate constant for O + H$_2$ = OH + H (R2) was revised to that recommended by Baulch et al. [20]. As noted in their assessment [20], the expression yields a better fit to lower temperature data than that of Sutherland et al. [91], which was the expression used in our previous model [12]. The two expressions [20,91] yield rate constants within 15% above 1500 K, but that of [20] is 50% lower at 1000 K. The rate expression from [20] used here results in a slower reaction in flow reactor speciation and lean flame conditions compared to that of [91] used in our previous model.

A number of recent studies have focused on the H$_2$O$_2$ consumption reactions, H$_2$O$_2$(+M) = OH + OH(+M) (R15) [87,92–94] and OH + H$_2$O$_2$ = HO$_2$+ H$_2$O (R19) [92]. Hong et al. [87,92] performed simultaneous H$_2$O and OH absorption measurements of H$_2$O$_2$/O$_2$/H$_2$O/Ar mixtures behind reflected shock waves; they derived k_{15} and k_{19} values by fitting a model to the experimental data. More recently, Sellevåg et al. [93] conducted ab initio transition-state-theory-based master equation calculations and Troe [94] performed weak collision modeling analyses based on an ab initio potential for (R15). Both studies [93,94] fitted $\langle \Delta E \rangle$ values to match available experimental data. Troe [94] regards that the two theoretical studies [93,94] represent the experimental data

within their scatter equally well, though we find that predictions of the present model using k_{15} from Troe [94] yield better agreement than that of Sellevåg et al. [93] with the experimental data of Hong et al. [87,92] at combustion-relevant temperatures. In fact, predictions of the present model that use the k_{15} expression from Troe [94] actually represent the experimental data of Hong et al. [87,92] better than predictions of the present model that use the k_{15} expression that Hong et al. derive from their data (see Fig. 13 later in this paper). As such, the present model uses the rate constant expression from Troe [94], which also includes falloff treatment and third-body efficiencies for He, O_2, N_2, CO_2, H_2O, and H_2O_2. Third-body efficiencies for H_2 and CO relative to N_2 from our previous model [12], scaled by 1.5 for compatibility with the present expression for Ar, are used here.

The rate constant expression for k_{19} proposed by Hong et al. [87] is adopted here. Their expression is a dual-Arrhenius-expression fit to their measurements from 1020 to 1460 K and previous measurements from 250 to 400 K. As mentioned above, predictions of the present model reproduce well the experimental data of Hong et al. [87], from which they derive k_{19} values (see Fig. 13 later in this paper).

INVESTIGATIONS OF NEGLECTED REACTIONS

The effects of the following often-neglected reactions on predictions of the validation targets were tested using rate constants from the studies indicated: $H + HO_2 = H_2O + O$ (X1) (see the $H + HO_2 =$ Products section above), $H + HO_2 + M = H_2O_2 + M$ (X2) [48], $OH + OH = H_2 + O_2$ (X3) [54], $H_2O + O = H_2 + O_2$ (X4) [54], $H_2O_2 + O = H_2O + O_2$ (X5) [20], and $O + OH + M = HO_2 + M$ (X6) (see below). Inclusion of reactions (X2)–(X5) using the rate constants indicated has no effect on predictions of the present validation set.

Proposed rate constants for (X6) are relatively limited and vary by two orders of magnitude. A review by Bahn [95] cites studies that propose values for k_{X6} of 1.2×10^{17} [96] and 5×10^{16} cm^6 mol^{-2} s^{-1} [97] deduced from static reactor experiments. In a more recent theoretical study, Germann and Miller [98] calculated rate constants for (X6) of approximately 10^{15} cm^6 mol^{-2} s^{-1} over a temperature range from 500 to 2000 K. While inclusion of the reaction using the highest proposed rate constant has a substantial effect on lean flames especially at high pressures (see [8]), inclusion of the reaction using the lower proposed rate constant has no effect on any of the model predic-

tions against the present validation targets. Notably, the rate constant of Germann and Miller [98] should actually be an upper bound due to their assumption of a strong collider. Sample master equation calculations, performed as part of the present study, support this—thereby corroborating that the reaction is not important for predicting the present validation set. Since the role of the reactions listed in Table III is either negligible or unclear for predictions of the present validation set, they are not included in the present model.

TRANSPORT

Given the large sensitivity to rate constants of reactions that consume H atoms, one might also suspect that modeling difficulties in high-pressure flames could be attributed to H atom diffusion coefficients. Predictions of the present kinetic model shown below employ an updated description of diffusive transport properties as compiled and distributed by Wang and coworkers [24]. The update includes improvements to the diffusion coefficients based on high-level quantum calculations [99] for the following pairs: H–He, H–H_2, H_2–He [100]; H–Ar [101]; N–H_2, N–N_2, H–O_2, O-O_2 [102]; H–N_2 [103]; H_2–N_2, N_2–N_2 [104]; and H_2–H_2 [105]. One of the more notable improvements is based on quantum calculations by Middha et al. [100] that include effects of transient-bound collisions for H–He and H–Ar pairs. Their calculations suggest a stronger temperature dependence of the H atom diffusion coefficient than that obtained using the conventional Lennard–Jones parameters available in the Sandia transport database [106]—yielding a diffusion coefficient that is about 20% higher at 1500 K. The updated transport model results in up to 10% differences in some flame speed targets—slightly faster at some conditions and slightly slower at others. Overall, the performance of the present kinetic model with the different transport treatments [24, 106] is similar.

MODEL PERFORMANCE

The present model was tested against a wide variety of combustion targets to evaluate its performance. The validation set here includes the full validation set from our previous models [12,47] as well as more recent measurements that have become available since the publication of the model of Li et al. [12]; many of these newly available measurements focus on high-pressure, low-temperature conditions. For example, new measurements have become available for speciation during H_2 oxidation [42], H_2O reaction with O_2 [71],

and H_2O_2 decomposition [87,92]; ignition delay times in shock tubes [10] and rapid compression machines (RCM) [11]; and flame speeds and mass burning rates [5–9].

The SENKIN code [107] was used to simulate experimental conditions in shock tubes, flow reactors, and rapid compression machines. The constant u–v assumption was employed to simulate shock tube conditions, and constant p–h assumption was employed to simulate flow reactor conditions, except where noted (see discussion below). For the simulation of ignition in rapid compression machines, an effective volume as a function of time is prescribed in SENKIN using parameters determined empirically to account for the nonadiabacity observed in such devices [108]. As opposed to other rapid compression studies (e.g., [109]) where effective compressed pressures and temperatures are used when modeling ignition assuming a constant volume adiabatic system, the entire compression and postcompression processes are modeled here. As shown by Mittal et al. [110], the compression stroke can have a considerable effect on induction chemistry, especially for short ignition delays; therefore, it is important to capture these effects in the modeling. For simulations of shock tube ignition delays where the shock tube is reported to behave nonideally (e.g., [10]) by exhibiting a monotonic pressure rise prior to the main ignition event, modeling is performed in a similar manner as that described above for RCMs by representing this pressure change through a time-varying effective volume, as described by Chaos and Dryer [111]. The PREMIX code [112], modified to accommodate the transport treatment and parameters recommended by Wang and coworkers [24], was used for flame calculations. Multicomponent and Soret effects were included. A minimum of 1000 grid points was imposed in the freely propagating flame calculations of burning velocities (and mass burning rates) and a minimum of 100 grid points in the burner-stabilized flame calculations for speciation to ensure grid-independent solutions. Comparisons of measurements and present model predictions are shown in Figs. 10–32.

As shown below, the present model and that of Li et al. [12] yield similar predictions for speciation and ignition delay times under homogeneous conditions for H_2/O_2 and H_2O/O_2 mixtures (in reasonable consistency with the experimental data), though the present model shows significant improvements in predictions of $H_2O_2/H_2O/O_2$ mixtures. Predictions using the present model reasonably reproduce the flame speed validation targets of Li et al. [12] and, most notably, show substantial improvements against recent high-pressure flame burning rate data. For the purposes of comparison, the recent H_2/O_2 model of Hong
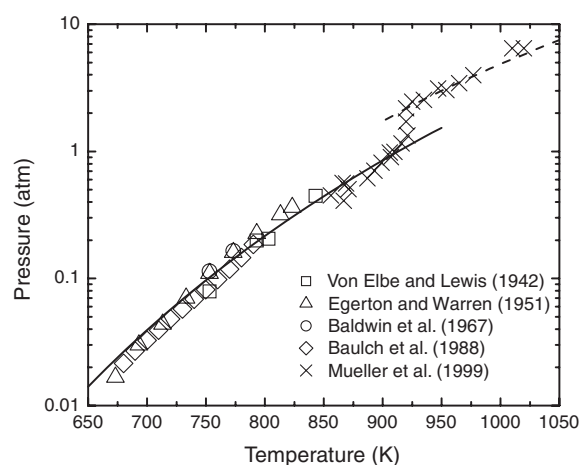
Figure 10 Second explosion limit experimental data for stoichiometric H_2/O_2 and $H_2/O_2/N_2$ mixtures. Symbols represent experimental determinations for H_2/O_2 mixtures composed of 67.7% H_2 and 33.3% O_2 in static reactors by von Elbe and Lewis [113] and Egerton and Warren [114] as well as a well-stirred reactor by Baulch et al. [116]; $H_2/O_2/N_2$ mixtures composed of 28% H_2, 14% O_2, and 58% N_2 in a static reactor by Baldwin et al. [115]; $H_2/O_2/N_2$ mixtures composed of 1% H_2, 0.5% O_2, and 98.5% N_2 in a flow reactor by Mueller et al. [47]. The data have been modified to take into account the third-body efficiencies of H_2 and O_2 relative to N_2, and efficiencies were taken from von Elbe and Lewis [113]. The solid line denotes the classical second limit criterion, $[M] = 2k_1/k_9$, computed using rate constant values from the present kinetic model for $M = N_2$. The dashed line denotes model results for the extended second limit, as described in the text.

et al. [19] was also tested against the full validation set used here. The model of Hong et al. [19] and the present model yield similar predictions for homogeneous targets (generally in very good agreement with the experimental data). However, the two models yield major differences in flame speed predictions at some higher pressure and/or more dilute conditions, where the present model shows significant improvements in reproducing the experimental data of [4,5,8]. We highlight comparisons where the two models exhibit significant differences in predictions in the Supporting Information (Figs. S8–S10). In addition, comparisons of predictions of several kinetic models [12–19,24] with the experimental data for nearly the entire validation set are shown in Figs. A-11 to A-S7 in the Supporting Information. Overall, predictions of the present model are generally in very good agreement with homogeneous targets and reproduce flame speeds within ~20% across a wide range of flame conditions (Figs. 20–24, 28, and 29); though they do not bring resolution to discrepancies with some flame speed data at very

low flame temperatures (below ∼1500 K in Figs. 25–27), for which a further study (both experimental and modeling) is warranted.

Explosion Limits

As part of the present validation, the ability of the model to properly reproduce reported hydrogen explosion limits is explored. Despite the fundamental nature of this validation target, H_2 kinetic modeling studies seldom consider it. However, proper representation of explosion limits provides a strong indication that a model correctly captures the balance between chain-branching and chain-terminating reactions as pressure and temperature conditions vary. Figure 10 shows explosion limit data from static reactors [113–115], a well-stirred reactor [116], and a flow reactor experiment [47]. In these experiments, temperature or pressure was varied until a rapid increase in the reaction rate was observed (e.g., a rapid rise in pressure or fuel consumption rate; see [47,113–116] for full details). The explosion limit is defined as the temperature and pressure at which this rapid increase in the reaction rate is observed. Such a behavior can be explained as follows.

At the lower pressures and temperatures of [113–116], HO_2 is unreactive on the diffusive-convective timescales of the system. Therefore, (R9) effectively removes active radicals whereas (R1) participates in a chain-branching cycle with (R2) and (R3) to essentially produce three H atoms for every H atom consumed. If (R1)–(R3) and (R9) are considered, and (R9) is assumed to be terminating, the overall branching ratio is responsible for the classical second explosion limit, $2k_1/(k_9 [M]) = 1$ [113]. Using the reaction rate constants for (R1) and (R9) of the present model, one can calculate the total concentration (i.e., pressure) that balances these two reactions, leading to the second explosion limit ($[M] = 2k_1/k_9$). As shown in Fig. 10, such calculations closely replicate the experimental data.

As pressure and temperature increase, Mueller et al. [47] observed a transition in the explosion limit to an "extended" second limit in the flow reactor. This arises due to experimental timescales and mixture dilution effects in the flow reactor as opposed to static reactors. At pressures above the third explosion limit and lower temperatures such that $2k_1/(k_9 [M]) < 1$, H_2O_2 formation from HO_2 and its subsequent decomposition and/or reaction allows for a chain-carrying reaction sequence that is thermally self-accelerative in contrast to the (faster) chain-explosive kinetics at higher temperatures [47]. Therefore, an extended second limit is manifested as a marked difference in characteristic reaction times [47]. However, as shown by Baldwin

and coworkers (e.g., [49]), consideration of the gas-phase consumption of HO_2 is additionally necessary to predict explosion limit behavior when HO_2 is reactive on timescales smaller than the diffusive-convective timescales of the system. The present model was used to compute characteristic reaction times for the conditions of Mueller et al. [47] at constant pressure and as a function of temperature for pressures between 1 and 10 atm. The characteristic reaction time was defined as $[H_2]_0/\{d[H_2]/dt\}_{max}$, where $[H_2]_0$ is the initial hydrogen concentration in the system and $\{d[H_2]/dt\}_{max}$ is the maximum hydrogen consumption rate. The temperature at which a rapid, marked decrease in the characteristic reaction time was observed (i.e., the explosion limit) is plotted in Fig. 10. Similar to the results obtained for the classical explosion limit, the calculations closely replicate the extended explosion limit data of Mueller et al. [47].

Speciation under Dilute Conditions

Figures 11 and 12 show comparisons of species time histories measured behind shock waves by Hanson and coworkers [42,43,117] and predicted using the present model and that of Li et al. [12] during H_2 oxidation. In a manner similar to that followed by the original authors who performed the experiments shown in Figs. 11 and 12, simulation results are shown here with time-shifts to match induction times. Time-shifts used here (–8 to
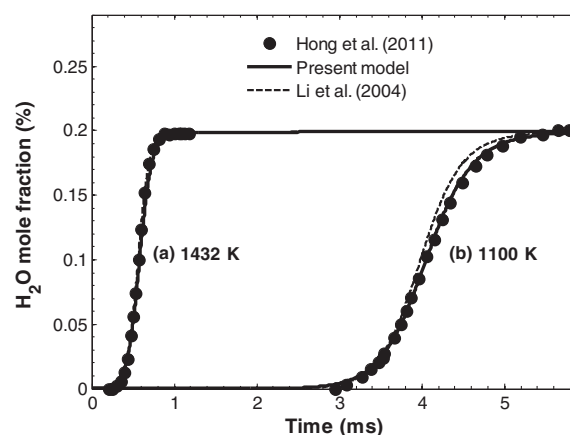
Figure 11 H_2O time histories behind shock waves in $H_2/O_2/Ar$ mixtures composed of (a) $H_2 = 0.9\%$, $O_2 = 0.1\%$, and Ar balance at 1.83 atm and 1472 K; (b) $H_2 = 2.9\%$, $O_2 = 0.1\%$, and Ar balance at 1.95 atm at 1100 K. Symbols represent experimental data from Hong et al. [42]; solid lines the present model; dashed lines the model of Li et al. [12]. Simulations performed using constant u–v and p–h assumptions yield identical predictions.
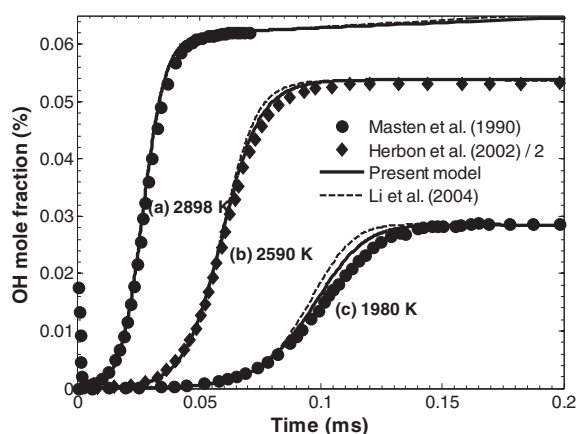
Figure 12 OH time histories behind shock waves in H$_2$/O$_2$/Ar mixtures composed of (a) H$_2$ = 1.10%, O$_2$ = 0.208%, and Ar balance at 1.98 atm and 2898 K; (b) H$_2$ = 0.4%, O$_2$ = 0.4%, and Ar balance at 1.075 atm and 2590 K; (c) H$_2$ = 5.0%, O$_2$ = 0.493%, and Ar balance at 0.675 atm and 1980 K. Symbols represent experimental data from Masten et al. [43] and Herbon et al. [117]; solid lines the present model; dashed lines the model of Li et al. [12].

920 μs) for the predictions shown appear reasonable in light of the discussion below.

As discussed in [42,43,117,118], experimental induction times can be highly sensitive to unmodeled effects of finite vibrational relaxation times and the presence of hydrocarbon impurities. Finite vibrational relaxation times require negative time-shifts, which have been estimated to be 6–12 μs for conditions typical of Figs. 11 and 12 (see comments in [117]). Hydrocarbon impurities are presumed to react with O$_2$ to initiate radical formation and accelerate the early reaction phase in a manner that requires positive time-shifts or introduction of ppb to ppm levels of H atoms to simulate the impurity (e.g., [42,117]). In fact, the effect of impurities was observed directly in the experiments of Hong et al. [71] despite frequent cleaning and vacuuming to 10^{-7} Torr between experiments (see discussion regarding Fig. 14). Without characterization and demonstrated repeatability of such impurity effects (or lack thereof) for each set of experimental conditions, induction times cannot be modeled properly.

However, while vibrational relaxation and hydrocarbon impurities are known to affect induction times, they are generally considered not to impact the subsequent reaction process where it is assumed that "memory of the initial process is lost" [42,119]. Such a conclusion is corroborated by a study from Yetter et al. [120], who demonstrated that chemical initiation processes strongly influence ignition delay times, but

have little influence on the observed rates of reaction thereafter.

The subsequent reaction, specifically the maximum slope, is considered to be governed by homogeneous kinetics of the fuel of interest. Sensitivity analysis for mole fractions of the measured species reveals high sensitivity to k_1 with additional influence from k_{10} and k_{11} at low temperatures as well as k_2 and k_3 in lean and near-stoichiometric mixtures. Predictions using the present model reasonably reproduce the H$_2$O time histories measured by Hong et al. [42] from 1100 to 1472 K and the OH time histories measured by Masten et al. [43] and Herbon et al. [117] from 1980 to 2898 K, all using the laser absorption technique. Furthermore, predictions using both models are consistent with the H time histories measured by Masten et al. [43] (e.g., see Fig. S1 in the Supporting Information) when the experimental results are scaled by $\pm$20% (well within the stated H-ARAS uncertainties due to $\pm$30% scatter in absorption cross-section calibration and $\pm$30% uncertainty in assuming a temperature independent cross section).

Figure 13 shows H$_2$O and OH time histories behind reflected shock waves measured by Hong et al. [87] and predictions using the present model and that of Li et al. [12] during H$_2$O$_2$ decomposition. Sensitivity analysis
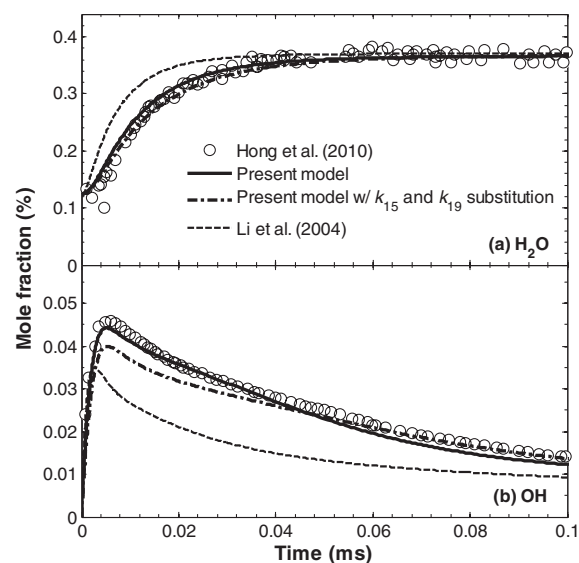

Figure 13 H$_2$O and OH time histories behind reflected shock waves in H$_2$O$_2$/H$_2$O/O$_2$/Ar mixtures composed of H$_2$O$_2$ = 0.25%, H$_2$O = 0.062%, O$_2$ = 0.031%, and Ar balance at 1398 K and 1.91 atm. Symbols represent experimental data from Hong et al. [87]; solid lines the present model; dashed–dotted lines the present model with k_{15} and k_{19} substituted from Hong et al. [87]; dashed lines the model of Li et al. [12]. Simulations were performed using a constant p–h assumption as used in Hong et al. [87].

[87] shows high sensitivity of computed H_2O and OH profiles primarily to k_{15} and k_{19} with additional influence from k_4 at longer times in the OH profiles and minor influences from k_{13} and k_{14}. Predictions using the present model closely replicate the observed H_2O and OH mole fractions. Also shown are predictions of the present model with substitution of the k_{15} and k_{19} values derived by Hong et al. [87] for the condition shown in Fig. 13 from a model fitted to the experimental data using a different kinetic model. While the predictions yield trends similar to those observed, they underpredict OH yields by ∼15%, indicating that k_{15} and k_{19} determination from the experimental data is dependent on the model used. The dependency of the rate constant determination for k_{15} and k_{19} on rate constants for secondary reactions demonstrates the utility of additionally providing the raw experimental data from elementary kinetic studies to allow for later reinterpretation when more accurate rate constants for secondary reactions become available. Nevertheless, predictions using the present model (that employs the k_{15} expression from Troe [94]) reproduce the experimental data well, indicating full consistency of the rate parameters used in the present model with the data; the predictions yield substantial improvements over those of Li et al. [12], which predicts a faster rate of H_2O production and OH decay than observed experimentally. While not shown here, a similar agreement is observed in comparisons against H_2O and OH time histories at 1057 and 1132 K from Hong et al. [79,84].

Figure 14 shows comparisons of OH time histories measured in $H_2O/O_2/Ar$ mixtures behind reflected shock waves by Hong et al. [71] and predicted by the present model and that of Li et al. [12]. The simulations include 0.7 ppm H atom as reactant, just as in Hong et al. [71], to simulate the effect of hydrocarbon impurities. In fact, they note that addition of similar H atom reactant mole fractions was necessary to reproduce OH time histories in shock-heated O_2/Ar mixtures. The effects of impurities persisted despite efforts to keep the shock tube clean and vacuuming the apparatus between experiments to 10^{-7} Torr [71]. Predictions using the present model are shown with ± 23 K temperature variation to illustrate the sensitivity of model predictions to reported temperature uncertainties. Sensitivity analysis [71] of computed OH mole fractions reveals highest sensitivity to k_{13} with minor contributions from k_1 and k_3 for the rate of OH formation after the initial induction period. Predictions using the present model and those of Li et al. [12] yield OH time histories that are consistent with the experimental results considering experimental uncertainties.

Figure 15 shows comparisons of H_2, O_2, and H_2O time histories measured in a variable pressure flow
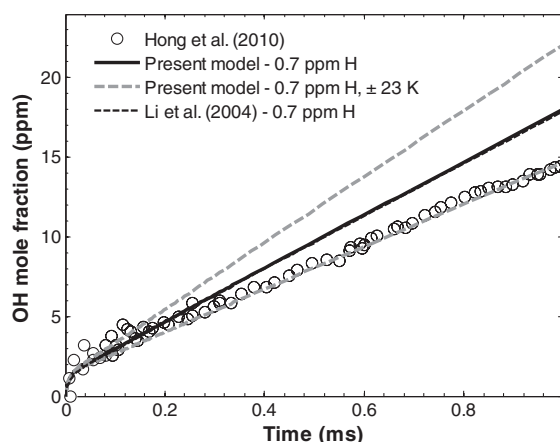
**Figure 14** OH time histories during H_2O decomposition in $H_2O/O_2/Ar$ mixtures at 1880 K and 1.74 atm. Symbols represent experimental data from Hong et al. [71]; solid lines the present model; thick dashed lines the present model with ± 23 K variation in initial temperature; thin dashed lines the model of Li et al. [12]. Simulations performed using constant p–h and u–v assumptions yield identical predictions; simulations performed using the present model and that of Li et al. [12] are indistinguishable.

reactor by Mueller et al. [47] and predicted by the present model and that of Li et al. [12]. Consistent with common practice, simulation results are time-shifted to match the point of 50% fuel consumption to remove effects of unmodeled processes inside the mixer–diffuser, including finite mixing times (see the Supporting Information in [121]). After the flow exits the mixer–diffuser, however, the reaction system can be reasonably simulated as a zero-dimensional, constant-pressure system [121]. Predictions against the experimental data of Mueller et al. [47] show considerable sensitivity to a number of reaction regimes, from branching reactions at lower pressures to HO_2 pathways at intermediate pressures to H_2O_2 pathways at higher pressures. Reasonable agreement is observed for the present model and that of Li et al. [12] with the experimental data in Fig. 15 as well as the rest of the experimental data from Mueller et al. [47] in Figs. S2–S5 provided in the Supporting Information.

Ignition Delay Times

Figure 16 shows comparisons of ignition delay times measured behind reflected shock waves by Pang et al. [10] and predicted by the present model (under various assumptions) and that of Li et al. [12] for dilute $H_2/O_2/Ar$ mixtures with a constant pressure rise, dP_5/dt, where P_5 is the test pressure established behind the reflected shock wave. Pang et al. [10] report
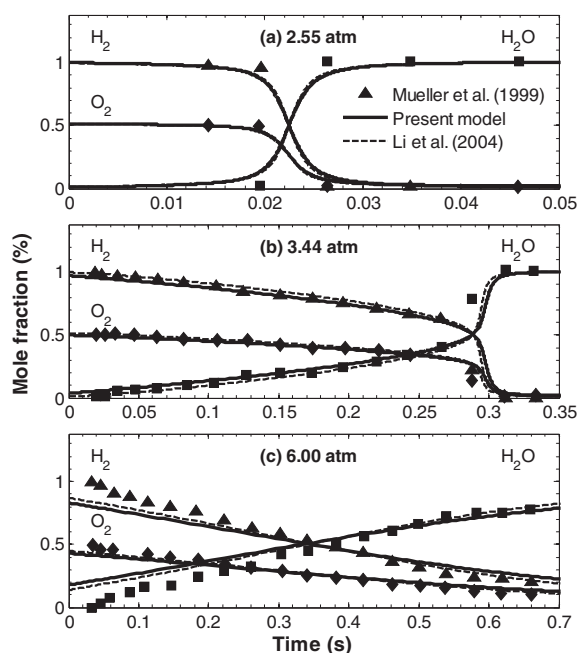
Figure 15 H$_2$, O$_2$, H$_2$O time histories in H$_2$/O$_2$/N$_2$ mixtures composed of H$_2$ = 1.01%, O$_2$ = 0.52%, and N$_2$ balance at 934 K at (a) 2.55 atm, (b) 3.44 atm, and (c) 6.00 atm in a variable pressure flow reactor. Symbols represent experimental data from Mueller et al. [47]; solid lines the present model; dashed lines the model of Li et al. [12].
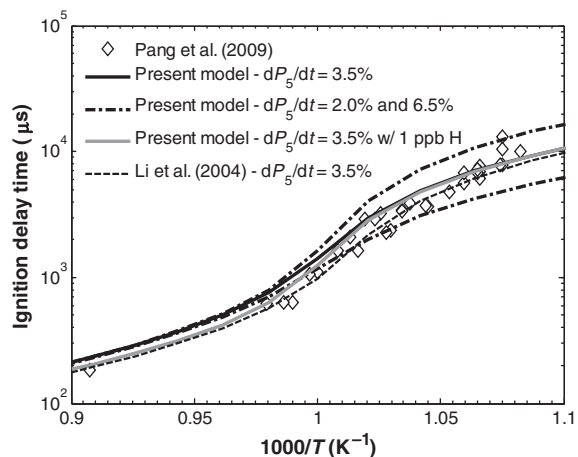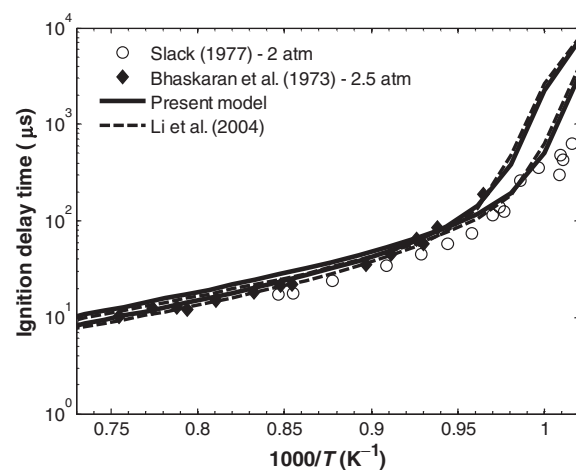

Figure 16 Ignition delay times at 3.5 atm of H$_2$/O$_2$/Ar mixtures composed of H$_2$ = 4%, O$_2$ = 2%, and Ar balance. Symbols represent experimental data from Pang et al. [10], and lines represent model predictions as indicated in the legend using the present model and that of Li et al. [12]. Ignition delay time is defined by a rapid increase in the pressure.

pressure rise rates behind the reflected shock waves for each experiment that range from 1.94 to 6.55% ms^{-1} with an average pressure rise rate across all the experiments of 3.5% ms^{-1}. Also shown are predictions of the present model with 3.5% ms^{-1} pressure rise rate with

1-ppb H atoms introduced as reactant, which results in up to ~20% shorter ignition delay times at temperatures higher than 1000 K. It is worth noting that 1-ppb H was introduced to match the induction time to account for hydrocarbon impurities in the simulation of similar conditions (1.95 atm and 1100 K) in the study of Hong et al. [42] in the same laboratory. Since radical concentrations in the early induction period were not reported to be quantified in Pang et al. [10] (nor in many other ignition delay time studies), it appears unclear whether the measured ignition delay times were affected by potential hydrocarbon impurities. Moreover, the ignition delay time predictions are sensitive to radical mole fractions (~1 ppb) that are likely below the detection limit of measurement techniques that we are aware of. Because of the sensitivity of ignition delay measurements to immeasurable impurities, as well as the effect of impurities suggested in several studies [42,43,71,117–119] and demonstrated in the experiments of Hong et al. [71] despite frequent cleaning and vacuuming to 10^{-7} Torr between experiments, we advise modelers to exercise caution in using ignition delay times for validation purposes and/or constraining rate constants.

Figures 17 and 18 show comparisons of ignition delay times measured in shock tubes [122–126] and predicted by the present model and that of Li et al. [12] for H$_2$/O$_2$/Ar mixtures under dilute and nondilute conditions. Reasonable agreement is observed between the experimental data and model predictions. Disagreement between predictions of both

Figure 17 Ignition delay times at 2 and 2.5 atm of H$_2$/O$_2$/N$_2$ mixtures composed of H$_2$ = 29.6%, O$_2$ = 14.8%, and N$_2$ balance. Symbols represent experimental data [122, 123]; solid lines the present model; dashed lines the model of Li et al. [12]. Ignition delay time is defined by a rapid increase in the pressure.
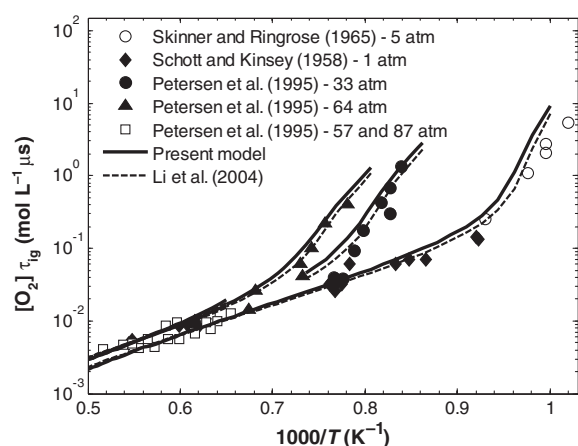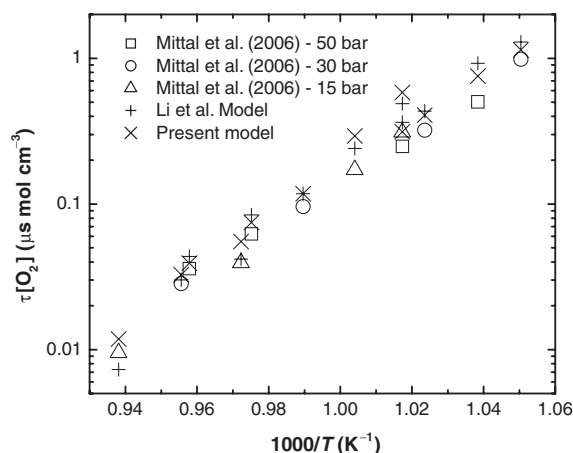
Figure 18 Ignition delay times of $H_2/O_2/Ar$ mixtures in shock tubes. Symbols represent experimental data for the following conditions: $H_2 = 8.0\%$, $O_2 = 2.0\%$ at 5 atm [124]; $H_2 = 1.0\%$, $O_2 = 2.0\%$ at 1 atm [125]; $H_2 = 2.0\%$, $O_2 = 1.0\%$, at 33, 57, 64, and 87 atm [126]. Solid lines represent the present model; dashed lines Li et al. [12]. Ignition delay time for the cases of [124] is defined by the maximum of OH concentration; for [125], as the time when the OH concentration reaches 1×10^{-6} mol/L; and for [126], by the maximum of d[OH]/dt.


Figure 19 Ignition delay times of $H_2/O_2/N_2/Ar$ (12.5/6.25/18.125/63.125 mol%) mixtures in a rapid compression machine. Open symbols represent experimental data [11] at the compressed pressures listed; crosses represent the present model and Li et al. [12].

models and the experimental data is observed at low temperatures where experimental ignition delay times are several times smaller than predictions. It should be noted that Pang et al. [10] conducted ignition delay measurements with similar fuel loadings, pressure, and temperature as the low-temperature data of Slack [122] (not shown here because pressure rise rates for these conditions are not provided in their paper). After the passage of the reflected shock wave, the measured pressure histories show a gradual, linear rise in the pressure, attributed to facility-dependent (fluid mechanical) effects; immediately prior to ignition, the pressure histories show a much higher pressure rise rate, attributed to preignition heat release [10]—presumably due to flame kernel growth in the boundary layer. Predictions from Pang et al. [10] based on their measured pressure histories, which serve to account for both facility-dependent effects and energy release, yield ignition delay times several times smaller than predictions using constant u–v assumptions [10,111]. Therefore, it appears likely that the low-temperature experimental data are influenced by similar facility-dependent and/or energy-release phenomena [111], for which insufficient information is provided to model properly.

Figure 19 shows ignition delays of $H_2/O_2/N_2/Ar$ mixtures collected in a rapid compression machine [11]. Predictions from the present model as well as from the model of Li et al. [12] are also shown. These measurements are particularly interesting as they were taken at temperatures below the extended second limit (see Fig. 10) for which ignition delays are generally too long to be captured in shock tubes. The present model performs well against the data, particularly at lower temperatures. Along with the results shown in Fig. 10, this further provides confidence in the ability of the present model to capture the ignition behavior at these high-pressure, low-temperature conditions.

Laminar Flame Speeds and Mass Burning Rates

Figure 20 shows comparisons of laminar burning velocities extracted from measurements of outwardly propagating flames using stretch correction [4,127–133] and those predicted by the present model and that of Li et al. [12]. A variety of data sets are shown in Fig. 20 to provide a context for interpreting burning velocity measurements. Uncertainties in the measured values are seldom quoted (e.g., 10% [129] and 12% [128] with 95% confidence), and scatter among data sets often exceeds what appear to be commonly expected uncertainties, which seem to be less than 10%. In Fig. 20, the data exhibit scatter that ranges from ~10 to 30%. Lower scatter is observed for near-stoichiometric mixtures, and higher scatter is observed for off-stoichiometric mixtures.
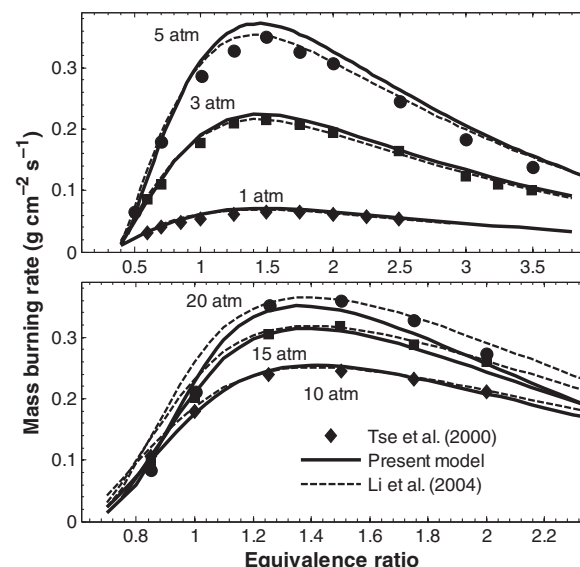
Predictions of the present model using the variety of stated conditions (such as initial temperature, initial pressure, and air composition) suggest that differences
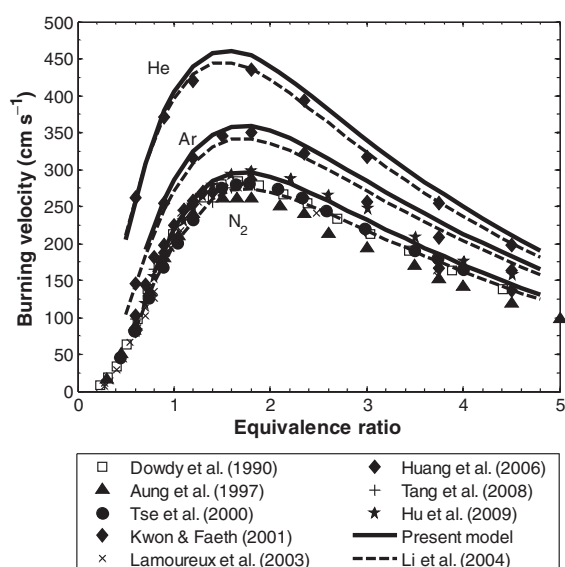
Figure 20   Laminar flame speed at 1 atm for H₂/O₂ diluted with N₂, Ar, or He with a dilution ratio of O₂:diluent = 1:3.76. Symbols represent experimental data [4,127–133]; solid lines the present model; dashed lines the model of Li et al. [12].

Figure 21   Laminar flame mass burning rate (a) at 1, 3, and 5 atm for H₂/O₂/He mixture with the dilution ratio O₂:He = 1:7 and (b) at 10, 15, and 20 atm for H₂/O₂/He mixture with the dilution ratio O₂:He = 1:11.5. Symbols represent experimental data from Tse et al. [4]; solid lines the present model; dashed lines the model of Li et al. [12].

in nominal conditions are insufficient to explain the level of scatter. While recent studies on effects of chamber confinement [134,135], ignition transient behavior [136], nonlinear stretch behavior, and extrapolation techniques [137–139] have suggested potential errors on the order of ~20%, these effects alone also appear insufficient to explain such large differences among some data sets. In fact, even different sets of data from the same laboratory using nearly identical equipment, conditions, and analysis procedures are different by –7 to +15% [128,129] and –3 to +22% [131, 133]. As such, the exact source(s) of disagreement among experimental values is (are) difficult to identify. It appears that unquantified effects from impurities (e.g., similar to Fe(CO)₅ presence in CO stored in steel bottles [75]), gas composition uncertainties (as quantified only in [8,9] to our knowledge), or other nonideal experimental effects that have received little attention might be responsible for the otherwise inexplicable discrepancies. For the purposes of the present study, we consider it sufficient to reproduce burning velocity measurements within ~20% at conditions where insufficient data are available for a particular set of conditions to establish reliability.

Figures 20 and 21 show comparisons of burning velocity measurements used for validation of our previous model [12] and those predicted by the present model and that of Li et al. [12]. The burning velocities were extracted from measurements of out-

wardly propagating flames using stretch correction for H₂/O₂/diluent flames of different equivalence ratios for various diluents at 1 atm [129] and H₂/O₂/He flames of different equivalence ratios at pressures from 1 to 20 atm [4]. Comparisons of the model predictions and experimental data reveal that the present model maintains reasonable fidelity to the previous validation targets of Li et al. [12] for various diluents and a wide range of equivalence ratios and pressures.
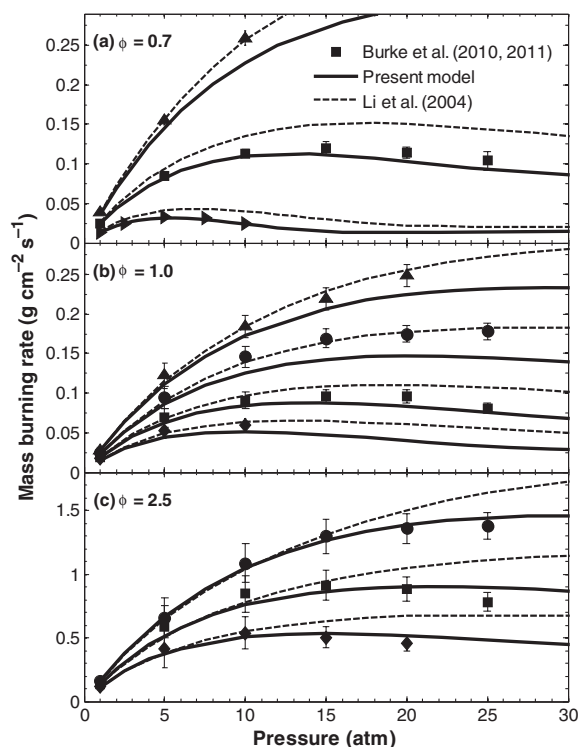
Figures 22–24 show comparisons of laminar mass burning rates extracted from more recent measurements of outwardly propagating flames using stretch correction by Burke et al. [8,9] and those predicted by the present model and that of Li et al. [12]. Figure 22 shows comparisons for the pressure dependence of H₂/O₂/He flames at an equivalence ratio of 0.3 with sufficient dilution to achieve a calculated adiabatic flame temperature near 1400 K as well as for an equivalence ratio of 0.85 with a flame temperature near 1600 K. Figure 23 shows comparisons for the pressure dependence of H₂/O₂/diluent flames of equivalence ratios 0.7, 1.0, and 2.5 at various dilution levels corresponding to different nominal flame temperatures from 1400 to 1800 K. Figure 24 shows comparisons for the equivalence ratio dependence at 1, 5, and 10 atm of lean H₂/O₂/He flames where dilution levels of each mixture were chosen to yield nominal flame temperatures near 1400 K (Fig. 24a) and 1600 K (Fig. 24b). The
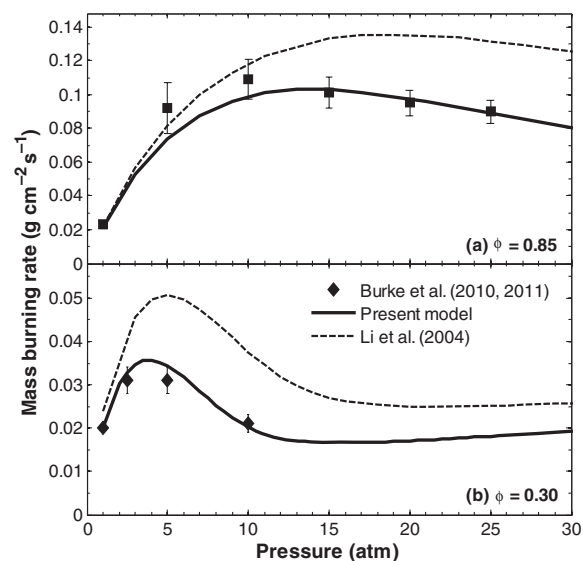
Figure 22 Pressure dependence of the laminar flame mass burning rate for (a) $H_2/O_2/He$ mixture of equivalence ratio 0.85 with dilution adjusted such that the adiabatic flame temperature is near 1600 K and (b) $H_2/O_2/He$ mixture of equivalence ratio 0.30 with dilution adjusted such that the adiabatic flame temperature is near 1400 K. Symbols represent experimental data from Burke et al. [8,9]; solid lines the present model; dashed lines the model of Li et al. [12].

Figure 23 Pressure dependence of the laminar flame mass burning rate at various flame temperatures for (a) $H_2/O_2/He$ mixtures of equivalence ratio 0.7 for flame temperatures of 1400, 1600, and 1800 K (ranked lowest to highest); (b) $H_2/O_2/He$ mixtures of equivalence ratio 1.0 for flame temperatures of 1500, 1600, 1700, and 1800 K (ranked lowest to highest); and (c) $H_2/O_2/Ar$ mixtures of equivalence ratio 2.5 for flame temperatures of 1500, 1600, 1700, 1800 K (ranked lowest to highest). The dilution level has been adjusted to achieve the different nominal flame temperatures. Symbols represent experimental data from Burke et al. [8,9]; solid lines the present model; dashed lines the model of Li et al. [12].

comparisons generally reveal significantly improved agreement between the experimental data and predictions using the present model compared to those of Li et al. [12]. While the model of Li et al. [12] predicts burning rates within a factor of two of those measured by Burke et al. [8,9], the present model predicts burning rates within 20% of those measured.

Figures 25 and 26 show comparisons of laminar burning velocities extracted from more recent measurements of outwardly propagating flames using stretch correction by Qiao et al. [7] and those predicted by the present model and that of Li et al. [12]. Figure 25 shows the dilution dependence of the laminar burning velocity for $H_2/air/diluent$ flames of equivalence ratio 1.0 (Fig. 25a) and 1.8 (Fig. 25b) with He, Ar, N_2, and CO_2 as the diluent at 1 atm. Figure 26 shows the dilution dependence of the laminar burning velocity for $H_2/air/diluent$ flames of equivalence ratio 1.0 with N_2 (Fig. 26a) or CO_2 (Fig. 26b) as the diluent at 0.5 atm. (Note that Figs. S6 and S7 provided in the Supporting Information display the same information with different axis scalings to focus on the higher dilution cases.) Experimental data and model predictions using the present model and that of Li et al. [12] agree within 20% at all conditions with diluent mole fractions less than 0.4 to 0.5 (corresponding to adiabatic

flame temperatures above ~1450 K). At the highest diluent mole fractions (corresponding to the lowest flame temperatures—near 1200 K), disagreement between predictions using the present model and that of Li et al. [12] and the experimental data reach a factor of two.

Figure 27 shows comparisons of laminar mass burning rates extracted from more recent measurements of outwardly propagating flames of H_2/air mixtures at 365 K from 1 to 10 atm by Bradley et al. [6] and those predicted by the present model and that of Li et al. [12]. Many of the burning velocities, particularly at higher pressures and leaner mixtures, were extracted from propagation speed measurements of wrinkled flames in a manner that requires a considerable correction. Experimental data and predictions using the present
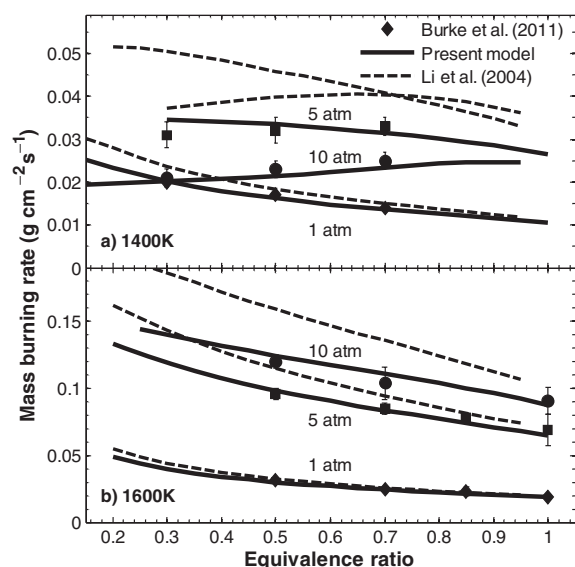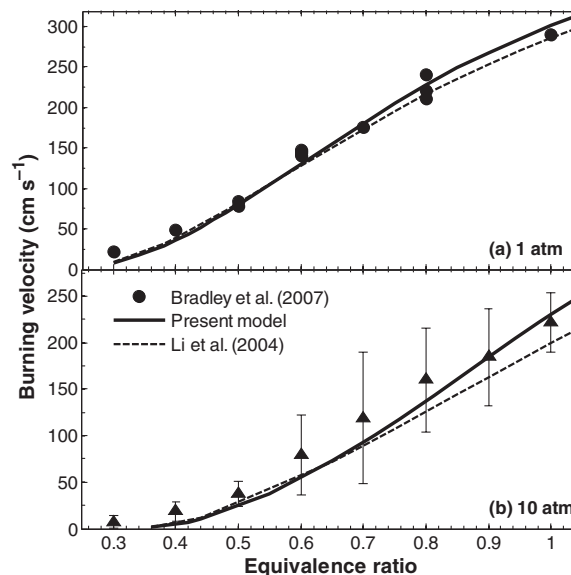
Figure 24 Equivalence ratio dependence of the laminar flame mass burning rate at various pressures for (a) H$_2$/O$_2$/He mixtures where the dilution level was adjusted for each equivalence ratio to achieve adiabatic flame temperatures near 1400 K and (b) H$_2$/O$_2$/He mixtures where the dilution level was adjusted for each case to achieve adiabatic flame temperatures near 1600 K. Symbols represent experimental data from Burke et al. [9]; solid lines the present model; dashed lines the model of Li et al. [12].
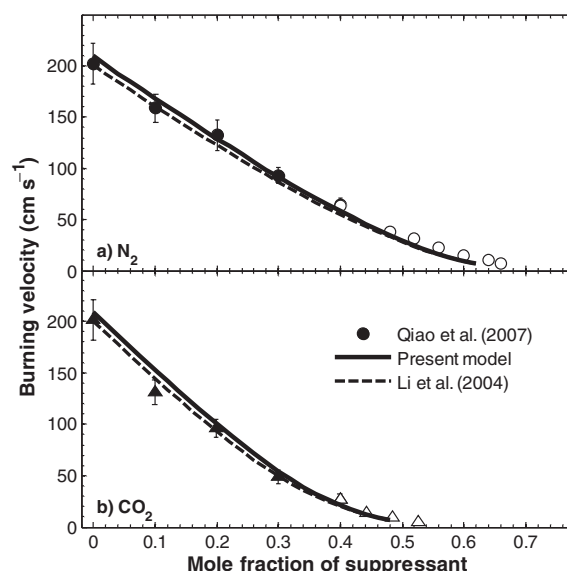
Figure 26 Dilution dependence of the laminar flame speed for various diluents in H$_2$/air/diluent mixtures of equivalence ratio 1.0 at 0.5 atm where the diluent is (a) N$_2$ and (b) CO$_2$. Closed symbols represent experimental data at normal gravity conditions, and open symbols represent experimental data at microgravity conditions from Qiao et al. [7]; solid lines the present model; dashed lines the model of Li et al. [12].
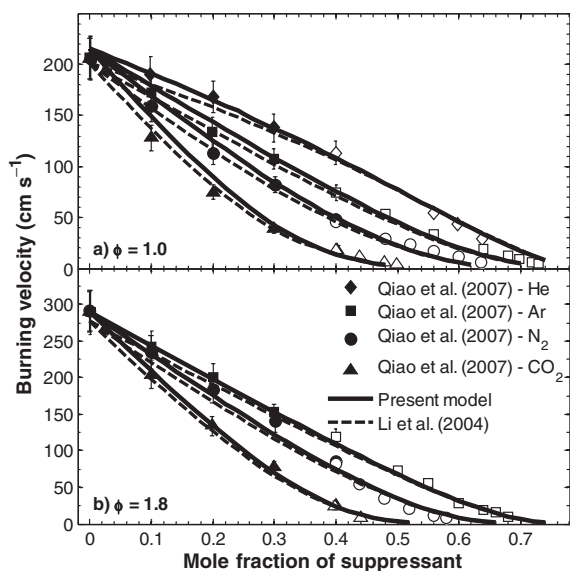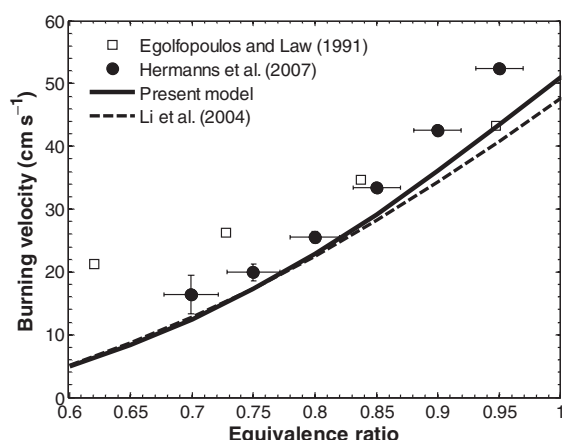

Figure 25 Dilution dependence of the laminar flame speed for various diluents in H$_2$/air/diluent mixtures of an equivalence ratio of (a) 1.0 and (b) 1.8 at 1 atm. Closed symbols represent experimental data at normal gravity conditions, and open symbols represent experimental data at microgravity conditions from Qiao et al. [7]; solid lines the present model; dashed lines the model of Li et al. [12].

Figure 27 Equivalence ratio dependence of the laminar burning velocity for H$_2$/air mixtures at 365 K at 1 and 10 atm. Symbols represent experimental data from Bradley et al. [6]; solid lines the present model; dashed lines the model of Li et al. [12].
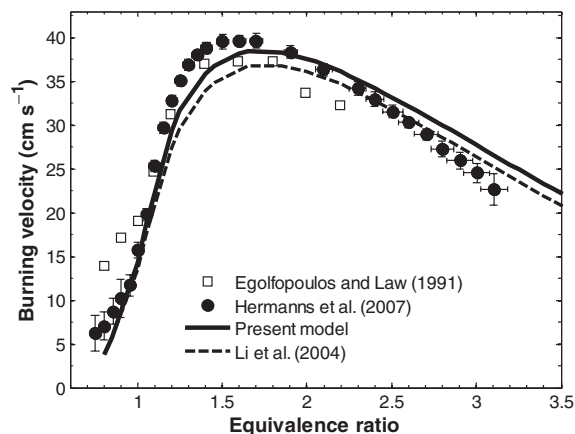
Figure 28 Oxygen mole fraction dependence of the laminar burning velocity for $H_2/O_2/N_2$ mixtures of equivalence ratio 1.058 at 298 K at 1 atm. Symbols represent experimental data from Hermanns et al. [5] and Egolfopoulos and Law [140]; solid lines the present model; dashed lines the model of Li et al. [12].

model and that of Li et al. [12] agree within 20%, or reported experimental error bars, except for equivalence ratios lower than 0.4 (corresponding to adiabatic flame temperatures less than ∼1500 K). Similar to comparisons of experiments from Qiao et al. [7] and predictions of the present model and that of Li et al. [12], the largest disagreement is observed at conditions that correspond to the lowest flame temperatures—reaching a factor of 2.7 at equivalence ratio 0.3 at 1 atm.

Figures 28 and 29 show comparisons of laminar burning velocities extracted from measurements

Figure 29 Equivalence ratio dependence of the laminar burning velocity for $H_2/O_2/N_2$ mixtures with $O_2/(O_2 + N_2)$ = 0.077 at 298 K at 1 atm. Symbols represent experimental data from Hermanns et al. [5] and Egolfopoulos and Law [140]; solid lines the present model; dashed lines the model of Li et al. [12].

of counterflow flames using stretch correction by Egolfopoulos and Law [140] and more recent measurements of burner-stabilized flames using the heat-flux method by Hermanns et al. [5] with those predicted by the present model and that of Li et al. [12]. Figure 28 shows comparisons for the oxygen fraction dependence of $H_2/O_2/N_2$ flames of equivalence ratio of 1.058 at 298 K and 1 atm. Figure 29 shows comparisons for the equivalence ratio dependence of $H_2/O_2/N_2$ flames with $O_2/(O_2 + N_2) = 0.077$ at 298 K and 1 atm. Similar to the experimental data for H_2/air mixtures at 1 atm and 298 K discussed above, the two available data sets [5,140] at the conditions of Figs. 28 and 29 exhibit significant differences, though here the differences reach a factor of two. It should be noted, though, that the data of Egolfopoulos and Law [140] should be further scrutinized. In interpreting their counterflow flame measurements, Egolfopoulos and Law used a linear relationship between a reference burning velocity and stretch to extrapolate to zero stretch and, thus, determine the unstretched laminar burning velocity. However, Tien and Matalon [141] later showed that as stretch approaches zero, this relationship is nonlinear, which can lead to errors in the determination of the unstretched laminar burning velocity. This error is small for Karlovitz numbers on the order of 0.1 [142], where the Karlovitz number represents the ratio of the characteristic residence time in the flame zone to that in the hydrodynamic zone. A small Karlovitz number is characteristic of "strong" flames for which flame speeds are relatively high and flame thicknesses are small. In Figs. 28 and 29, the data of Egolfopoulos and Law [140] represent Karlovitz number conditions on the order of unity; these are very weak flames, and the linear extrapolation technique can yield unstretched burning velocities that can considerably overestimate the actual value. In reevaluating the data of Egolfopoulos and Law, Vagelopoulos et al. [142] showed that for speeds lower than approximately 40 cm s^{-1} the approach of Egolfopoulos and Law overestimated the unstretched burning velocity by 10–50%. This explains the larger discrepancies seen in Figs. 28 and 29 among experimental data for highly diluted and lean flames.
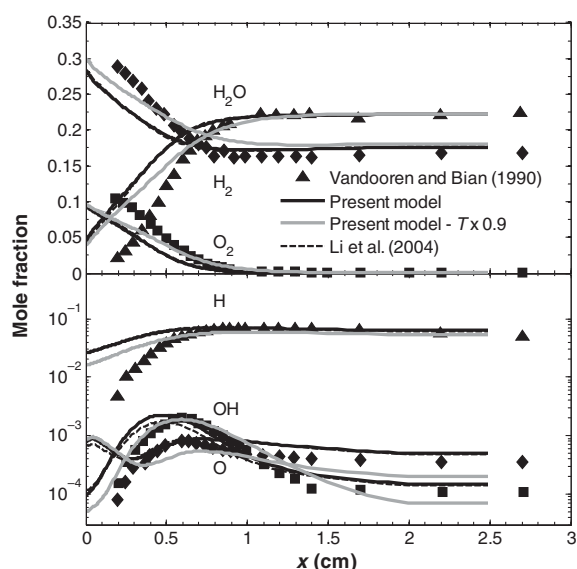
Predictions using both the present model and the model of Li et al. [12] reproduce the more recent burning velocity measurements of Hermanns et al. [5] over the full range of conditions studied within 20%. Interestingly, the predictions closely replicate the experimental data of Hermanns et al. [5] for $H_2/O_2/N_2$ flames of equivalence ratio of 1.058 for a wide range of oxygen fractions corresponding to flame temperatures from 1150 to 1590 K. However, while the predictions and the experimental data of Qiao et al. [7] for $H_2/O_2/N_2$ flames of equivalence ratio of 1.0 (see

Fig. 25a) are within 20% for dilution fractions up to 0.48 (corresponding to flame temperatures from 1490 to 2340 K), predictions and experimental data differ more substantially for higher dilution ratios, reaching a factor of two at a dilution fraction of 0.6 (corresponding to a flame temperature of 1240 K).

Based on the differences between the two data sets at the same conditions [5,140], the conflicting conclusions regarding model performance for similar near-stoichiometric mixtures [5,7], and the difficulties noted above in determining accurate flame speeds with some experimental techniques, it appears possible that burning velocity uncertainties are considerably higher for more highly dilute conditions. Further measurements at these highly dilute conditions to establish repeatability of experimental data would be important for resolving the source of the discrepancy.
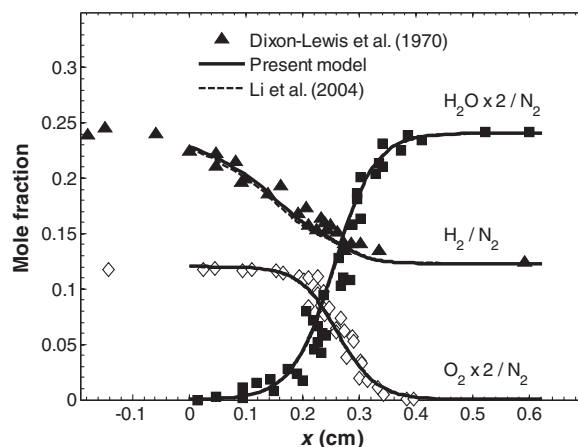
Speciation in Burner-Stabilized Flames

Figure 30 shows H$_2$, O$_2$, H$_2$O, H, O, and OH mole fractions in the flame structure of burner-stabilized, rich H$_2$/O$_2$/Ar flames at 0.47 atm measured by Vandooren and Bian [143] and predictions using the present model and that of Li et al. [12]. Consistent with common

practice, the simulations were conducted by prescribing the temperature profile measured experimentally to account for potential intrusive effects from the probe insertion into the flow [144]. The present model and that of Li et al. [12] predict nearly identical speciation profiles in the flame structure. To aid in interpretation of the comparison, various tests were conducted to ascertain the sensitivity of the predictions to kinetics, transport, and boundary conditions. Predictions using the present model with the A-factors of (R1) and (R9) (two of the most sensitive reactions indicated for all species mole fractions) independently increased by 50% yield negligible differences in the predicted profiles. Predictions with and without inclusion of multicomponent transport and Soret effect, with the updated transport from Wang and coworkers [24] and with conventional Lennard-Jones transport [106], and with the collision diameter of H atom varied by a factor of two yield somewhat larger differences. However, predictions conducted with the prescribed temperature profile uniformly decreased by 10% (shown in Fig. 30) yield differences larger than any of the above-mentioned perturbations in the kinetic and transport models. A recent assessment of the effect of probe intrusion on burner-stabilized flames [144] indicates that uncertainties of ±100 to 200 K are typical for the measured temperature profile. As such, it appears that disagreement between the experimental data and the model predictions is more likely attributable to uncertainties in boundary conditions than to uncertainties in the kinetic or transport models.

Figures 31 and 32 show further comparisons of predictions using the present model and those of Li et al.

Figure 30 Species profiles in a burner-stabilized flame of an H$_2$/O$_2$/Ar mixture composed of H$_2$ = 39.7%, O$_2$ = 10.3%, and Ar = 50.0% at 0.047 atm. Symbols represent experimental data from Vandooren and Bian [143]; solid lines the present model; gray lines the present model with specified temperature uniformly decreased by 10%; dashed lines the model of Li et al. [12]. Predictions of the present model and Li et al. [12] are indistinguishable except for the OH mole fraction.

Figure 31 Species profiles in a burner-stabilized flame of an H$_2$/O$_2$/N$_2$ mixture composed of H$_2$ = 18.8%, O$_2$ = 4.6%, and N$_2$ = 76.6% at 1 atm. Symbols represent experimental data from Dixon-Lewis et al. [145]; solid lines the present model; dashed lines the model of Li et al. [12]. Predictions of the present model and Li et al. [12] are indistinguishable.
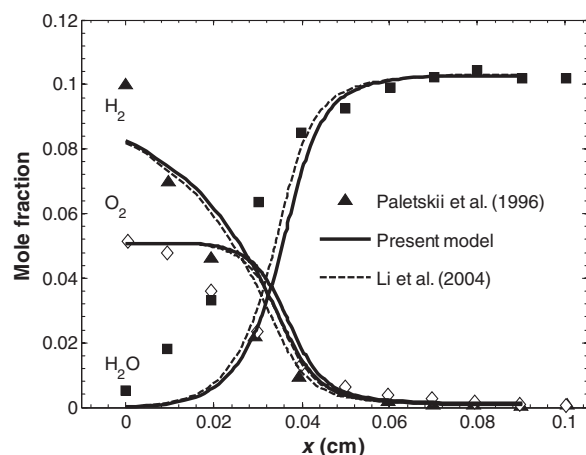
Figure 32 Species profiles in a burner-stabilized flame of an $H_2/O_2/Ar$ mixture composed of $H_2 = 10\%$, $O_2 = 5\%$, and $Ar = 85\%$ at 10 atm. Symbols represent experimental data from Paletskii et al. [146]; solid lines the present model; dashed lines the model of Li et al. [12].

[12] with speciation data for burner-stabilized flames measured by Dixon-Lewis et al. [145] in rich $H_2/O_2/N_2$ flames at 1 atm and measured by Paletskii et al. [146] in rich $H_2/O_2/Ar$ flames at 10 atm. Both of these flame conditions show similar sensitivities to kinetics, transport, and boundary conditions to that of Vandooren and Bian [143] discussed above. Given the small flame thickness in the 10-atm measurements (0.7 mm) from Paletskii et al. [146], the data are further complicated by limited spatial resolution of 0.1 mm, as discussed in Konnov [14].

CONCLUSIONS

An updated H_2/O_2 kinetic model that incorporates recent improvements in the rate constant and transport treatment from fundamental studies as well as improves agreement with recent combustion data has been formulated and tested. Major remaining sources of uncertainties affecting predictions of relevant combustion behavior were identified in both the parameters and the assumptions of the kinetic model. With regard to model parameters, present uncertainties in the temperature and pressure dependence of rate constants for HO_2 formation and consumption reactions are demonstrated to substantially affect predictive capabilities at high-pressure/low-temperature conditions. With regard to model assumptions, calculations were performed in several instances to investigate the effects of reactions/processes that have not received much attention previously, including the pressure dependence of $H + O_2 = OH + O$ (R1), temperature dependence

of the $H + HO_2$ reaction channels, significance of $O + OH + M = HO_2 + M$ (X6), and nonlinear mixture rules for $H + O_2(+M) = HO_2(+M)$ (R9) in multicomponent bath gases. At present, the role of $H + HO_2 = H_2O + O$ (X1) in combustion modeling remains unclear. Furthermore, it appears that characterization of nonlinear bath-gas mixture rule behavior for $H + O_2(+M) = HO_2 (+M)$ in multicomponent bath gases might be necessary to predict high-pressure flame speeds within $\sim 15\%$.

The model was tested against all of the previous validation targets of Li et al. [12] as well as new targets from a number of recent studies. Special attention was devoted to establishing a context for evaluating model performance against the experimental data by careful consideration of uncertainties in measurements, initial conditions, and physical model assumptions. For example, ignition delay times in shock tubes are suspected to be affected by potential hydrocarbon impurities, which have been suggested to accelerate early radical pool growth in shock tube speciation studies. In addition, speciation predictions in burner-stabilized flames are found to be more sensitive to uncertainties in experimental boundary conditions than to uncertainties in kinetics and transport. Predictions using the present model adequately reproduce targets from the validation set of Li et al. [12] and show substantially improved agreement against recent high-pressure flame speed and shock tube speciation measurements; though, they do not completely resolve discrepancies with flame speed measurements at very low flame temperatures, where further studies (both experimental and modeling) are warranted.

Comparisons of predictions of several kinetic models [12–19,24] with the experimental data for nearly the entire validation set used here can be found in Figs. A-11 to A-S7 in the Supporting Information.

The current kinetic model associated with this paper is provided in an electronic form compatible with CHEMKIN II in the Supporting Information. The model also appears on our laboratory Web site (http://www.princeton.edu/mae/people/faculty/dryer/homepage/combustion_lab/). Consideration of future revisions and comparisons with data not discussed in this paper will also appear on this site.

## APPENDIX : LIMITATIONS OF RATE CONSTANT FORMS FOR UNIMOLECULAR/RECOMBINATION REACTIONS

The limitations of two standard rate constant treatments presently available in CHEMKIN software for

unimolecular/recombination reactions with high-pressure falloff are discussed in this section. The treatments are both based on the Troe formulation but differ in terms of what parameters can be specified for different bath gas components as well as when the summation across all bath gas components takes place in the calculation. In the "single expression" treatment, as it is referred to here, one expression is provided for the reaction, viz.,

$$A + B \,(+M) = AB \,(+M) \qquad (A1)$$
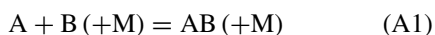
and only one set of parameters is specified for $k_0(T)$, $k_\infty(T)$, and $F_c(T)$ for all bath gases. The reaction rate constant, $k(T, P, [M]_{eff})$, for the mixture is then calculated based on an effective bath gas concentration, $[M]_{eff} = \sum_i \varepsilon_i [M_i]$, where ε_i, the third-body efficiency for each bath gas component, i, is specified. However, the single-expression treatment allows for neither the temperature dependence of the low-pressure limit nor the pressure dependence in the falloff regime to be specified for each bath gas.

In the "multiple-expression" treatment, separate expressions for the reaction, viz.

$$A + B \,(+M_1) = AB \,(+M_1) \qquad (A1.1)$$

$$\ldots \qquad (A1.i)$$

$$A + B \,(+M_n) = AB \,(+M_n) \qquad (A1.n)$$
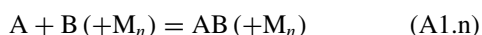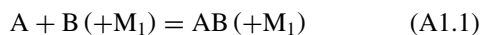
and sets of parameters are specified for $k_{0,i}(T)$, $k_{\infty,i}(T)$, and $F_{c,i}(T)$ for all n bath gas components. The reaction rate constant, $k(T, P, [M_i])$, for each bath gas component is calculated, and the overall reaction rate constant for the mixture is calculated by summing the rate constants for each bath gas component. The treatment allows for the temperature dependence of the low-pressure limit and the pressure dependence in the falloff regime to be specified for each bath gas (though it should be noted that sufficient data to justify the bath-gas specific expressions are available for only a limited number of reactions). However, the multiple-expression treatment essentially considers the separate expressions to be independent reactions such that the occurrence of falloff effects for one expression does not impact the evaluation of rate constants for the other expressions. (See the discussion regarding Fig. 3 for more information.)

BIBLIOGRAPHY

1. Westbrook, C. K.; Dryer, F. L. Prog Energy Combust Sci 1984, 10, 1–57.
2. Richards, G. A.; Casleton, K. H.; Weiland, N.T. In Synthesis Gas Combustion: Fundamentals and Applications; T. C. Lieuwen, V. Yang, R. A. Yetter (Eds.); CRC Press, Taylor & Francis Group: Boca Raton, FL, 2009; pp. 193–222.
3. Chaos, M.; Burke, M. P.; Ju, Y.; Dryer, F. L. In Synthesis Gas Combustion: Fundamentals and Applications; T. C. Lieuwen, V. Yang, R. A. Yetter (Eds.); CRC Press, Taylor & Francis Group: Boca Raton, FL, 2009; pp. 29–70.
4. Tse, S. D.; Zhu, D. L.; Law, C. K. Proc Combust Inst 2000, 28, 1793–1800.
5. Hermanns, R. T. E.; Konnov, A. A.; Bastiaans, R. J. M., de Goey, L. P. H. Energy Fuels 2007, 21, 1977–1981.
6. Bradley, D.; Lawes, M.; Liu, K.; Verhelst, S.; Woolley, R. Combust Flame 2007, 149, 162–172.
7. Qiao, L.; Gu, Y.; Dahm, W. J. A.; Oran, E. S.; Faeth, G. M. Combust Flame 2007, 151, 196–208.
8. Burke, M. P.; Chaos, M.; Dryer, F. L.; Ju, Y. Combust Flame 2010, 157, 618–631.
9. Burke, M. P.; Dryer, F. L.; Ju, Y. Proc Combust Inst 2011, 33, 905–912.
10. Pang, G. A.; Davidson, D. F.; Hanson, R. K. Proc Combust Inst 2009, 32, 181–188.
11. Mittal, G.; Sung, C.-J.; Yetter, R. A. Int J Chem Kinet 2006, 38, 516–529.
12. Li, J.; Zhao, Z.; Kazakov, A.; Dryer, F. L. Int J Chem Kinet 2004, 36, 566–575.
13. Davis, S. G.; Joshi, A.; Wang, H.; Egolfopoulos, F. N. Proc Combust Inst 2005, 30, 1283–1292.
14. Konnov, A. A. Combust Flame 2008, 152, 507–528.
15. Sun, H. Y.; Yang, S. I.; Jomaas, G.; Law, C. K. Proc Combust Inst 2007, 31, 439–446.
16. O'Connaire, M.; Curran, H. J.; Simmie, J. M.; Pitz, W. J.; Westbrook, C. K. Int J Chem Kinet 2004, 36, 603–622.
17. Saxena, P.; Williams, F. A. Combust Flame 2006, 145, 316–323.

18. Smith, G. P.; Golden, D. M.; Frenklach, M.; Moriarty, N. W.; Eiteneer, B.; Goldenberg, M.; Bowman, C. T.; Hanson, R. K.; Song, S.; Gardiner, W. C., Jr.; Lissianski, V. V.; Qin, Z. GRI-MECH 3.0. Available at http://www.me.berkeley.edu/gri_mech/, accessed 2009.

19. Hong, Z.; Davidson, D. F.; Hanson, R. K. Combust Flame 2011, 158, 633–644.

20. Baulch, D. L.; Bowman, C. T.; Cobos, C. J.; Cox, R. A.; Just, T.; Kerr, J. A.; Pilling, M. J.; Stocker, D.; Troe, J.; Tsang, W.; Walker R.W.; Warnatz, J. J Phys Chem Ref Data 2005, 34, 757–1397.

21. Hippler, H.; Troe, J.; Willner, J. J Chem Phys 1990, 93, 1755–1760.

22. Kappel, Ch.; Luther, K.; Troe, J. Phys Chem Chem Phys 2002, 4, 4392–4398.

23. Burke, M. P.; Klippenstein, S. J.; Harding, L. B. In 2011 Fall Eastern States Section Technical Meeting of the Combustion Institute, University of Connecticut, Storrs, CT, October 9–12, 2011.

24. Wang, H.; You, X.; Joshi, A. V.; Davis, S. G.; Laskin, A.; Egolfopoulos, F. N.; Law, C. K. USC Mech Version II. High-Temperature Combustion Reaction Model of $H_2/CO/C_1$–C_4 Compounds. Available at http://ignis.usc.edu/USC_Mech_II.htm; May 2007, accessed 2009.

25. Michael, J. V.; Su, M.-C.; Sutherland, J. W.; Carroll, J. J.; Wagner, A. F. J Phys Chem A 2002, 106, 5297–5313.

26. Troe, J. Proc Combust Inst 2000, 28, 1463–1469.

27. Bates, R. W.; Golden, D. M.; Hanson, R. K.; Bowman, C. T. Phys Chem Chem Phys 2001, 3, 2337–2342.

28. Hahn, J.; Krasnoperov, L.; Luther, K.; Troe, J. Phys Chem Chem Phys 2004, 6, 1997–1999.

29. Sellevåg, S. R.; Georgievskii, Y.; Miller, J. A. J Phys Chem A 2008, 112, 5085–5095.

30. Troe, J.; Ushakov, V. G. J Chem Phys 2008, 128, 204307.

31. Harding, L. B.; Troe, J.; Ushakov, V. G. Phys Chem Chem Phys 2000, 2, 631–642.

32. Fernandes, R. X.; Luther, K.; Troe, J.; Ushakov, V. G. Phys Chem Chem Phys 2008, 10, 4313–4321.

33. Cobos, C. J.; Hippler, H.; Troe, J., J Phys Chem 1985, 89, 342–349.

34. Janik, I.; Bartels, D. M.; Martin, T. W.; Jonah, C. D. J Phys Chem A 2007, 111, 79–88.

35. Miller, J. A., personal communication, 2010.

36. Troe, J. Ber Bunsen-Ges Phys Chem 1980, 84, 829–834.

37. Dove, J. E.; Halperin, S.; Raynor, S. J Chem Phys 1984, 81, 799–811.

38. Troe, J. J Phys Chem 1979, 83, 114–126.

39. Troe, J. Ber Bunsen-Ges Phys Chem 1983, 87, 161–169.

40. Gilbert, R. G.; Luther, K.; Troe, J. Ber Bunsen-Ges Phys Chem 1983, 87, 169–177.

41. Zhang, P.; Law, C. K.; Int J Chem Kinet 2009, 41, 727–734.

42. Hong, Z.; Davidson, D. F.; Barbour, E. A.; Hanson, R. K. Proc Combust Inst 2011, 33, 309–316.

43. Masten, D. A.; Hanson, R. K.; Bowman, C. T. J Phys Chem 1990, 94, 7119–7128.

44. Pirraglia, A. N.; Michael, J. V.; Sutherland, J. W.; Klemm, R. B. J Phys Chem 1989, 93, 282–291.

45. Hessler, J. P. J Phys Chem A 1998, 102, 4517–4526.

46. Westmoreland, P. R.; Howard, J. B.; Longwell, J. P.; Dean, A. M. AIChE J 1986, 32, 1971–1979.

47. Mueller, M. A.; Kim, T. J.; Yetter, R. A.; Dryer, F. L. Int J Chem Kinet 1999, 31, 113–125.

48. Mousavipour, S. H.; Saheb, V. Bull Chem Soc Jpn 2007, 80, 1901–1913.

49. Baldwin, R. R.; Walker, R. W. J Chem Soc, Faraday Trans I 1979, 75, 140–154.

50. Baldwin, R. R.; Fuller, M. E.; Hillman, J. S.; Jackson, D.; Walker, R. W. J Chem Soc, Faraday Trans I 1974, 70, 635–641.

51. Sridharan, U. C.; Qiu, L. X.; Kaufman, F. J Phys Chem 1982, 86, 4569–4574.

52. Keyser, L. F. J Phys Chem 1986, 90, 2994–3003.

53. Michael, J. V.; Sutherland, J. W.; Harding, L. B.; Wagner, A. F. Proc Combust Inst 2000, 28, 1471–1478.

54. Karkach, S. P.; Osherov, V. I. J Chem Phys 1999, 110, 11918–11927.

55. Klippenstein, S. J. J Chem Phys 1992, 96, 367–371.

56. Klippenstein, S. J.; East, A. L. L.; Allen, W. D. J Chem Phys 1996, 105, 118–139.

57. Harding, L. B.; Georgievskii Y.; Klippenstein, S. J. J Phys Chem A 2005, 109, 4646– 4656.

58. Klippenstein, S. J.; Georgievskii Y.; Harding, L. B. Phys Chem Chem Phys 2006, 8, 1133–1147.

59. Jasper, A. W.; Klippenstein, S. J.; Burke, M. P. In 7th International Conference on Chemical Kinetics, Massachusetts Institute of Technology, Cambridge, MA, July 10–14, 2011.

60. DeMore, W. B. J Phys Chem 1979, 83, 1113–1118.

61. DeMore, W. B. J Phys Chem 1982, 86, 121–126.

62. Sridharan, U. C.; Qiu, L. X.; Kaufman, F. J Phys Chem 1984, 88, 1281–1282.

63. Keyser, L. F. J Phys Chem 1988, 92, 1193–1200.

64. Lii, R.-R.; Corse, R. A.; Sauer, M. C.; Gordon, S. J Phys Chem 1980, 84, 813–817.

65. Cox, R. A.; Burrows, J. P.; Wallington, T. J. Chem Phys Lett 1981, 84, 217–221.

66. Kurylo, M. J.; Klais, O.; Laufer, A. H. J Phys Chem 1981, 85, 3674–3678.

67. Braun, M.; Hofzumahaus, A.; Stuhl, F. Ber Bunsenges Phys Chem 1982, 86, 597–602.

68. Hippler, H.; Troe, J. Chem Phys Lett 1992, 192, 333–337.

69. Hippler, H.; Neunaber, H.; Troe, J. J Chem Phys 1995, 103, 3510–3516.

70. Srinivasan, N. K.; Su, M.-C.; Sutherland, J. W.; Michael, J. V.; Ruscic, B. J Phys Chem A 2006, 110, 6602–6607.

71. Hong, Z.; Vasu, S. S.; Davidson, D. F.; Hanson, R. K. J Phys Chem A 2010, 114, 5520–5525.

72. Goodings, J. M.; Hayhurst, A. N. J Chem Soc, Faraday Trans 1988, 84, 745–762.

73. Peeters, J.; Mahnen, G. Proc Combust Inst 1973, 14, 133–146.

74. Harding, L. B.; Klippenstein, S. J. unpublished.

75. Chaos, M.; Dryer, F. L. Combust Sci Technol 2008, 180, 1053–1096.

76. Rasmussen, C. L.; Hansen, J.; Marshall, P.; Glarborg, P. Int J Chem Kinet 2008, 40, 454–480.

77. Sivaramakrishnan, R.; Comandini, A.; Tranter, R. S.; Brezinsky, K.; Davis, S. G.; Wang, H. Proc Combust Inst 2007, 31, 429–437.

78. Baulch, D. L.; Cobos, C. J.; Cox, R. A.; Esser, C.; Frank, P.; Just, Th.; Kerr, J. A.; Pilling, M. J.; Troe, J.; Walker, R. W.; Warnatz, J. J Phys Chem Ref Data 1992, 21, 411–734.

79. Patrick, R.; Pilling, M. J. Chem Phys Lett 1982, 91, 343–347.

80. Lightfoot, P. D.; Veyret, B.; Lesclaux, R. Chem Phys Lett 1988, 150, 120–126.

81. Tsang, W.; Hampson, R. F. J Phys Chem Ref Data 1986, 15, 1087–1222.

82. Srinivasan, N. K.; Michael, J. V.; Int J Chem Kinet 2006, 38, 211–219.

83. Bedjanian, Y.; Le Bras, G.; Poulet, G. J Phys Chem A 1999, 103, 7017–7025.

84. Wooldridge, M. S.; Hanson, R. K.; Bowman, C. T. Int J Chem Kinet 1994, 26, 389–401.

85. Lifshitz, A.; Michael, J. V. Proc Combust Inst 23, 1991, 59–67.

86. Sutherland, J. W.; Patterson, P. M.; Klemm, R. B. Proc Combust Inst 23, 1991, 51–57.

87. Hong, Z.; Cook, R. D.; Davidson, D. F.; Hanson, R. K. J Phys Chem A 2010, 114, 5718–5727.

88. Keyser, L. F. J Phys Chem 1982, 86, 3439–3446.

89. Brune, W. H.; Schwab, J. J.; Anderson, J. G. J Phys Chem 1983, 87, 4503–4514.

90. Fernández-Ramos, A.; Varandas, A. J. C. J Phys Chem A 2002, 106, 4077–4083.

91. Sutherland, J. W., Michael, J. V.; Pirraglia, A.; Nesbitt, F. L.; Klemm, R. B. Proc Combust Inst 1986, 21, 929–941.

92. Hong, Z.; Farooq, A.; Barbour, E. A.; Davidson, D. F.; Hanson, R. K. J Phys Chem A 2009, 113, 12919–12925.

93. Sellevåg, S. R.; Georgievskii, Y.; Miller, J. A. J Phys Chem A 2009, 113, 4457–4467.

94. Troe, J. Combust Flame 2001, 158, 594–601.

95. Bahn, G. S. Reaction Rate Compilation for the H–O–N System; Gordon and Breach: New York, 1968; p. 113.

96. Kretschmer, C. B. Aerojet-General Corporation Report 1611 (AFOSR-TR-59-62), May 1959, AD 217008.

97. Petersen, H. L.; Kretschmer, C. B. Aerojet-General Corporation Report TN-38 (AFOSR-TN-60-1478), November 1960, AD 283044.

98. Germann, T. C.; Miller, W. H. J Phys Chem A 1997, 101, 6358–6367.

99. Middha, P.; Wang, H. Combust Theory Modell 2005, 9, 353–363.

100. Middha, P.; Yang, B.; Wang, H. Proc Combust Inst 2002, 29, 1361–1369.

101. Middha, P.; Wang, H. In 2002 Annual Meeting of American Institute of Chemical Engineers, Indianapolis, IN, November 3–8, 2002.

102. Stallcop, J. R.; Partridge, H.; Levin, E. Phys Rev A. 2001, 64, 042722.

103. Stallcop, J. R.; Partridge, H.; Walch, S. P.; Levin, E. J Chem Phys 1992, 97, 3431–3436.

104. Stallcop, J. R.; Partridge, H.; Levin, E. Phys Rev A. 2000, 62, 062709.

105. Stallcop, J. R.; Levin, E.; Partridge, H. J Thermophys Heat Trans 1998, 12, 514–519.

106. Kee, R. J.; Dixon-Lewis, G.; Warnatz, J.; Coltrin, M. E.; Miller, J. A. Report SAND86-8246; Sandia National Laboratories: Albuquerque, NM, 1986.

107. Lutz, A. E.; Kee, R. J.; Miller, J. A. Report SAND-87-8248; Sandia National Laboratories: Albuquerque, NM, 1988.

108. Mittal, G.; Sung, C.-J. Combust Sci Technol 2007, 179, 497–530.

109. He, X.; Donovan, M. T.; Zigler, B. T.; Palmer, T. R.; Walton, S. M.; Wooldridge, M. S.; Atreya, A. Combust Flame 2005, 142, 266–275.

110. Mittal, G.; Chaos, M.; Sung, C.-J.; Dryer, F. L. Fuel Proc Technol 2008, 89, 1244–1254.

111. Chaos, M.; Dryer, F. L. Int J Chem Kinet 2010, 43, 143–150.

112. Kee, R. J.; Grcar, J. F.; Smooke, M. D.; Miller, J. A. Report SAND85-8240; Sandia National Laboratories: Albuquerque, NM, 1985.

113. von Elbe, G.; Lewis, B., J Chem Phys 1942, 10, 366–393.

114. Egerton, A.; Warren, D. R., Proc R Soc A—Math Phys 1951, 204, 465–476.

115. Baldwin, R. R.; Jackson, D.; Walker, R. W.; Webster, S. J. Trans Faraday Soc 1967, 63, 1676–1686.

116. Baulch, D. L.; Griffiths, J. F.; Pappin, A. J.; Sykes, A. F. Combust Flame 1988, 73, 163–185.

117. Herbon, J. T.; Hanson, R. K.; Golden, D. M.; Bowman, C. T. Proc Combust Inst 2002, 29, 1201–1208.

118. Yu, C.-L.; Frenklach, M.; Masten, D. A.; Hanson, R. K.; Bowman, C. T. J Phys Chem 1994, 98, 4770–4771.

119. Ryu, S.; Hwang, S. M.; Rabinowitz, M. J. J Phys Chem 1995, 99, 13984–13991.

120. Yetter, R. A.; Dryer, F. L.; Rabitz, H. Combust Flame 1985, 59, 107–133.

121. Zhao, Z.; Chaos, M.; Kazakov, A.; Dryer, F. L. Int J Chem Kinet 2008, 40, 1–18.

122. Slack, M. W. Combust Flame 1977, 28, 241.

123. Bhaskaran, K. A.; Gupta, M. C. Just, Th. Combust Flame 1973, 21, 45.

124. Skinner, G. B.; Ringrose, G. H. J Chem Phys 1965, 42, 2190.

125. Schott, G. L.; Kinsey, J. L. J Chem Phys 1958, 29, 1177.

126. Petersen, E. L.; Davidson, D. F.; Rohrig, M.; Hanson, R. K. AIAA 95-3113, 31st AIAA/ASME/SAE/ASEE Joint Propulsion Conference and Exhibit, San Diego, CA, 1995.

127. Dowdy, D. R.; Smith, D. B.; Taylor, S. C. Proc Combust Inst 1991, 23, 325–332.

128. Aung, K. T.; Hassan, M. I.; Faeth, G. M. Combust Flame 1997, 109, 1.

129. Kwon, O. C.; Faeth, G. M. Combust Flame 2001, 124, 590.

130. Lamoureux, N.; Djebaïli-Chaumeix, N.; Paillard, C.-E. Exp Thermal Fluid Sci 2003, 27, 385–393.

131. Huang, Z.; Zhang, Y.; Zenga, K.; Liu, B.; Wang, Q.; Jiang, D. Combust Flame 2006, 146, 302–311.

132. Tang, C.; Huang, Z.; Jin, C.; He, J.; Wang, J.; Wang, X.; Miao, H. Int J Hydrogen Energy 2008, 33, 4906–4914.

133. Hu, E.; Huang, Z.; He, J.; Jin, C.; Zheng, J. Int J Hydrogen Energy 2009, 34, 4876–4888.

134. Burke, M. P.; Chen, Z.; Ju, Y.; Dryer, F. L. Combust Flame 2009, 156, 771–779.

135. Chen, Z.; Burke, M. P.; Ju, Y. Combust Theory Modell 2009, 13, 343–364.

136. Chen, Z.; Burke, M. P.; Ju, Y. Proc Combust Inst 2009, 32, 1253–1260.

137. Kelley, A. P.; Law, C. K. Combust Flame 2009, 156, 1844–1851.

138. Halter, F.; Tahtouh, T.; Mounaïm-Rousselle, C. Combust Flame 2010, 157, 1825–1832.

139. Chen, Z. Combust Flame 2011, 158, 291–300.

140. Egolfopoulos, F.; Law, C. K. Proc Combust Inst 1991, 23, 333–340.

141. Tien, J. H.; Matalon, M. Combust Flame 1991, 84, 238–248.

142. Vagelopoulos, C. M.; Egolfopoulos, F. N.; Law, C. K. Proc Combust Inst 1994, 25, 1341–1347.

143. Vandooren, J.; Bian, J. Proc Combust Inst 1990, 23, 341–346.

144. Struckmeier, U.; Oβwald, P.; Kasper, T.; Böhling, L.; Heusing, M.; Köhler, M.; Brockhinke, A.; Kohse-Höinghaus, K. Z Phys Chem 2009, 223, 503–537.

145. Dixon-Lewis, G.; Sutton, M. M.; Williams, A. Proc R Soc London A 1970, 317, 227–234.

146. Paletskii, A. A.; Kuibida, L. V.; Bolshova, T. A.; Korobeinichev, O. P.; Fristrom, R. M. Combust Explos Shock Waves 1996, 32, 245–250.

147. Michael, J. V.; Sutherland, J. W. J Phys Chem 1988, 92, 3853–3857.